

Early-warning the compact-to-dendritic transition via spatiotemporal learning of two-dimensional growth images

Hyunjun Jang,¹ Chung Bin Park^{†,2} Jeonghoon Kim^{‡,3} and Jeongmin Kim^{*4}

¹⁾*Department of Energy Engineering, Korea Institute of Energy Technology (KENTECH), Naju 58330, Republic of Korea*

²⁾*Department of Chemistry Education, Korea National University of Education, Cheongju, 28173, Republic of Korea*

³⁾*Microsoft, Redmond, WA, 98052, USA*

⁴⁾*Department of Chemistry Education and Graduate Department of Chemical Materials, Pusan National University, Busan 46241, Republic of Korea*

(Electronic mail: [†]cbpark@knue.ac.kr [‡]jeonghoonkim@microsoft.com ^{*}jeongmin@pusan.ac.kr)

(Dated: 16 February 2026)

Transitions between distinct dynamical regimes are ubiquitous in nonequilibrium systems. As a prototypical example, deposition growth is often accompanied by irreversible morphological instabilities. Forecasting such transitions from pre-transition configurations remains fundamentally challenging, as early precursors are weak, spatially heterogeneous, and masked by inherent fluctuations. Here, we investigate compact-to-dendritic transitions (CDTs) in a two-dimensional particle-based electrodeposition model and formulate a horizon-based early-warning task using trajectory-resolved transition points. We demonstrate that anticipating the CDT is intrinsically a spatiotemporal problem: neither static morphological descriptors nor temporal learning applied to predefined features alone yields reliable predictive signals. In contrast, end-to-end learning of jointly optimized spatial and temporal representations from growth images enables robust anticipation across a wide range of prediction horizons. Analysis of the learned latent dynamics reveals the emergence of a low-dimensional surrogate variable that tracks progressive morphological destabilization and undergoes reorganization near the transition. We further show that the learned spatiotemporal representation exhibits limited but systematic transferability across reaction-rate conditions, with predictive performance degrading as the inference condition departs from the training condition, consistent with changes in the latent-state dynamics. Overall, our results establish a general formulation for forecasting incipient instabilities in nonequilibrium interfacial growth, with implications for the predictive monitoring and control of pattern-forming driven systems.

I. INTRODUCTION

Sudden transitions between distinct dynamical regimes are a hallmark of nonequilibrium systems^{1–8}. Such transitions are often accompanied by qualitative changes in structure, transport, or reactivity, and arise across a wide range of contexts, including pattern-forming instabilities, percolation and fracture processes, and driven interfacial growth^{9–14}. Nonequilibrium driven systems frequently exhibit emergent fluctuations and spatiotemporal pattern formation that cannot be inferred reliably from static observables alone^{15–18}. While the states before and after a transition are often well characterized within established physical frameworks, anticipating the onset of a transition remains fundamentally more challenging^{19–32}. This difficulty arises because early-stage precursors are typically weak, spatially heterogeneous, and masked by intrinsic fluctuations^{19,31,33–41}. Accordingly, identifying predictive indicators and early-warning signals for critical transitions has become a central objective across many complex systems^{42–45}.

Electrochemical dendritic deposition provides a prototypical and technologically important realization of this general problem^{35,46–52}. The gradual evolution from compact, spatially uniform deposition to highly branched dendritic growth constitutes a nonequilibrium interfacial instability with direct consequences for device safety, performance, and lifetime^{19,53}. This instability originates from the competition between diffusive transport and interfacial reaction kinetics and can be

characterized by a dimensionless Damköhler number^{13,53–57},

$$\text{Da} = \frac{kL}{D}, \quad (1)$$

where k is an effective reaction rate, D the ionic diffusivity, and L a characteristic interfacial length scale. In the diffusion-dominated regime ($\text{Da} \ll 1$), incoming particles sufficiently sample the interface prior to incorporation, leading to compact growth^{58–62}. When reaction kinetics locally outpace diffusive relaxation ($\text{Da} \gtrsim 1$), interfacial perturbations are amplified, giving rise to dendritic morphologies⁴⁷. Consequently, even for fixed reaction and transport parameters, a compact-to-dendritic transition (CDT) is generically expected as growth proceeds, although its precise onset depends sensitively on stochastic growth dynamics^{63–68}. These considerations have motivated strategies such as pulsed or modulated charging protocols that attempt to delay dendritic growth by dynamically altering the effective reaction–diffusion balance^{65–68}.

Classical frameworks such as diffusion-limited aggregation and related reaction–diffusion models successfully rationalize the morphology and scaling behavior across this transition^{65–67}. In particular, Eden-type growth represents the reaction-limited, compact extreme, whereas diffusion-limited aggregation (DLA) corresponds to the diffusion-controlled dendritic limit^{69,70}. However, during early growth the deposit remains globally compact, and the instability manifests only through weak, localized interfacial fluctuations^{46–48,71,72}. As a result, predicting the eventual onset of dendritic growth from

early-stage configurations remains difficult, due to stochasticity and intrinsic interfacial heterogeneity^{19,20,73–76}. This suggests that early-warning of dendritic instability requires detecting subtle and evolving spatiotemporal correlations, rather than identifying static morphological signatures alone^{33–35}. These challenges are further compounded by limited experimental access to buried interfacial dynamics, motivating the use of physics-based simulations and synthetic image data as controlled testbeds^{35,51,56,77,78}.

Recent advances demonstrate that machine learning and reinforcement learning can autonomously learn effective representations and control strategies in complex physical systems, ranging from turbulent flows and active matter to self-assembly and quantum dynamics^{79–84}. In interfacial growth problems, image-based learning is particularly attractive because it can implicitly encode multiscale morphological features and collective fluctuations that are difficult to capture with handcrafted descriptors^{85–90}. When combined with physically grounded models, such approaches naturally lend themselves to early-warning and control in driven nonequilibrium systems, where timely intervention is required to prevent irreversible instabilities^{33–35}. Related data-driven methods have also been explored for optimizing electrochemical and battery processes, including fast-charging protocols and degradation-aware control^{91–93}.

For example, Kumar *et al.*⁸⁵ developed a convolutional LSTM-based, image-driven framework to predict the spatiotemporal evolution of dendritic copper electrodeposition from real-time microscopy data, demonstrating forecasting of future growth morphologies without explicit physical modeling^{48,94–97}. Such studies highlight the ability of deep learning to capture complex growth patterns and morphological variability^{35,85,86}. However, most existing approaches focus on next-frame or future-sequence prediction and lack an explicit, physically grounded formulation of early-warning for the compact-to-dendritic transition from pre-transition configurations^{47,98,99}.

In this work, we study compact-to-dendritic transitions (CDTs) in a particle-based electrodeposition model using image-based spatiotemporal learning combined with physics-based growth simulations⁴⁷. Using trajectory-resolved transition points as ground truth, we formulate CDT forecasting as binary event prediction over a future horizon E from pre-transition image sequences. By benchmarking models that disentangle or jointly learn spatial representation and temporal integration^{19,100}, we show that reliable early-warning near the alarm boundary requires both effective temporal integration and end-to-end learning of joint spatial and temporal representations. Models that satisfy both (CNN–GRU and CNN–TCN) achieve consistently strong performance across wide prediction horizons, whereas approaches lacking either component degrade significantly. Analysis of the learned dynamics reveals that the CNN–GRU organizes pre-transition information into a structured latent evolution, supporting the interpretation of the hidden state as a low-dimensional surrogate for progressive morphological destabilization^{96,97,101}. Transfer across reaction-rate conditions is limited but systematic, and fine-tuning restores performance without evidence of

accelerated learning. Our results establish a practical and generalizable framework for forecasting incipient morphological instabilities in driven nonequilibrium pattern-forming systems.

II. PARTICLE-BASED MODEL AND COMPACT-TO-DENDRITIC TRANSITION

We model electrodeposition in two dimensions using a particle-based aggregation model that captures the competition between diffusion and surface reaction, a minimal description known to reproduce both compact and dendritic growth morphologies⁴⁷. Growth proceeds through repeated cycles of Brownian diffusion of reactive particles in the electrolyte domain followed by probabilistic sticking upon contact with the growing aggregate, representing electrochemical reduction at the interface. The reaction probability is controlled by a rate constant k , which interpolates between reaction-limited (compact) and diffusion-limited (dendritic) growth. All simulations are performed using a publicly available implementation with parameters identical to those in Ref.¹⁰². Further algorithmic details of the reaction-diffusion model are provided in Appendix A.

A. Compact-to-dendritic transition (CDT)

The fractal dimension d_f provides a quantitative measure of aggregate morphology through the scaling relation

$$N(R) \sim R^{d_f}, \quad (2)$$

where $N(R)$ denotes the number of deposited particles contained within a distance R from the aggregate center. Physically, values of $d_f \approx 2$ correspond to compact, space-filling growth, whereas lower values ($d_f \approx 1.7$) are characteristic of branched or dendritic morphologies^{65–67}. The evolution of d_f therefore serves as a sensitive indicator of structural changes during aggregation. We compute d_f numerically following Ref. 47:

$$d_f = \frac{d \log_{10} N}{d \log_{10}(kR_g/D)}, \quad (3)$$

where R_g is the radius of gyration of the aggregate. This differential definition captures local deviations from global scaling and is therefore well suited for detecting morphological transitions during nonequilibrium growth for each growth trajectory.

The onset of dendritic growth for each trajectory is identified by a critical radius R_c ,

$$R_c = \arg \max_{R_g} \left(\frac{d \log_{10} N}{d \log_{10}(kR_g/D)} \right), \quad (4)$$

which marks the CDT and follows the scaling relation $R_c \sim D/k$. Across this CDT transition, the effective fractal dimension d_f decreases gradually, reflecting a morphological crossover from compact to dendritic growth. For image-based

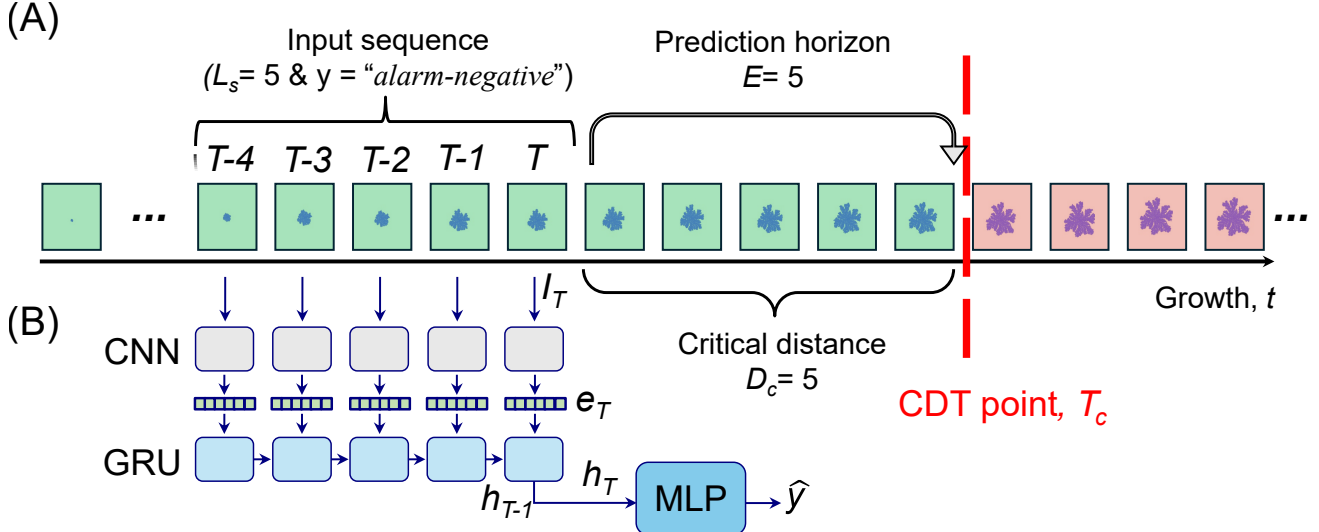


FIG. 1. Setup for early-warning learning. (A) Schematic illustration of temporal sequence construction and early-warning labeling. At a reference temporal index $t = T$, the model observes an input sequence of L_s past growth images, $\{I_{T-L_s+1}, \dots, I_T\}$. The compact-to-dendritic transition (CDT) occurs at T_c , and the critical distance is defined as $D_c = T_c - T$. The label y is assigned as alarm-positive if $T_c \in [T, T + E]$, i.e., if the transition occurs within a future prediction horizon of length E , and as alarm-negative otherwise. (B) Architecture of the CNN-GRU model for end-to-end spatiotemporal learning. CNN extracts spatial feature representations e_t from each image, GRU models their temporal evolution into a hidden state h_T , and an MLP outputs the predicted label \hat{y} (alarm-positive or alarm-negative).

analysis, instead of the ensemble-averaged value of R_c , we compute a sequence-specific R_c for each growth trajectory. This trajectory-resolved definition serves as a ground-truth reference for subsequent compact-dendritic classification. Some figures show the ensemble-averaged R_c as a visual reference unless noted. We note that accurate determination of the ensemble-averaged R_c requires extensive ensemble averaging over many independent growth trajectories, which is not the primary objective of this work.

In addition to the fractal dimension d_f , other physical quantities provide complementary geometric measures of morphological evolution across the CDT⁴⁷ (see Appendix C for calculation details). For instance, the interfacial length L_{int} characterizes the degree of interfacial roughness and branching of the deposited aggregate and is defined as the perimeter of the aggregate boundary in two dimensions. In the compact growth regime prior to the CDT, the interface remains relatively smooth and L_{int} scales linearly with aggregate size, $L_{\text{int}} \sim R_g$ ^{33–35}. Beyond the transition, the emergence of branching and interfacial instabilities leads to a nontrivial scaling,

$$L_{\text{int}} \sim R_g^{d_i}, \quad (5)$$

where the interfacial exponent d_i is empirically found to lie in the range $1.66 \lesssim d_i \lesssim 1.760$, reflecting the increased geometric complexity of the dendritic interface. To obtain a dimensionless quantity with behavior analogous to d_f , we define the normalized interfacial length as

$$\tilde{L}_{\text{int}} = \frac{L_{\text{int}} R_g}{A}, \quad (6)$$

where A is the cluster area. This quantity increases in the dendritic post-CDT regime.

III. EARLY-WARNING TASK AND MODELS

Particle configurations from deposition simulations are mapped onto binary images $I_t \in \mathbb{R}^{H \times W}$ at regular growth intervals corresponding to $\Delta N = 10^3$ newly deposited particles, thereby defining an updated temporal index t . This procedure yields 10^3 temporal image frames along each growth trajectory. We emphasize that the index t represents the growth progression in the strict sense, not directly the physical time of the evolving system, which is not tracked in the deposition simulations employing algorithmic techniques for efficient sampling⁴⁷. Nevertheless, the early-warning framework developed in this work can be straightforwardly applied to any genuinely time-evolving system. Unless otherwise stated, the results presented here focus on the case $H \times W = 32 \times 32$, for which the interfacial morphologies remain clearly identifiable (see Fig. A1). Further details of the image processing pipeline, including image construction, normalization, and scaling procedures, are provided in Appendix B.

The early-warning task is formulated as binary event-prediction on the future morphology of temporal sequences. At temporal index $t = T$, the model observes an input window $\{I_{T-L_s+1}, \dots, I_T\}$ and predicts whether the CDT will occur within a future horizon of length E . An input sequence, whose images all belong to the pre-CDT regime, is labeled *alarm-positive* if $T_c \in [T, T + E]$ and *alarm-negative* otherwise, where T_c is the critical time when $R_g = R_c$. Equivalently,

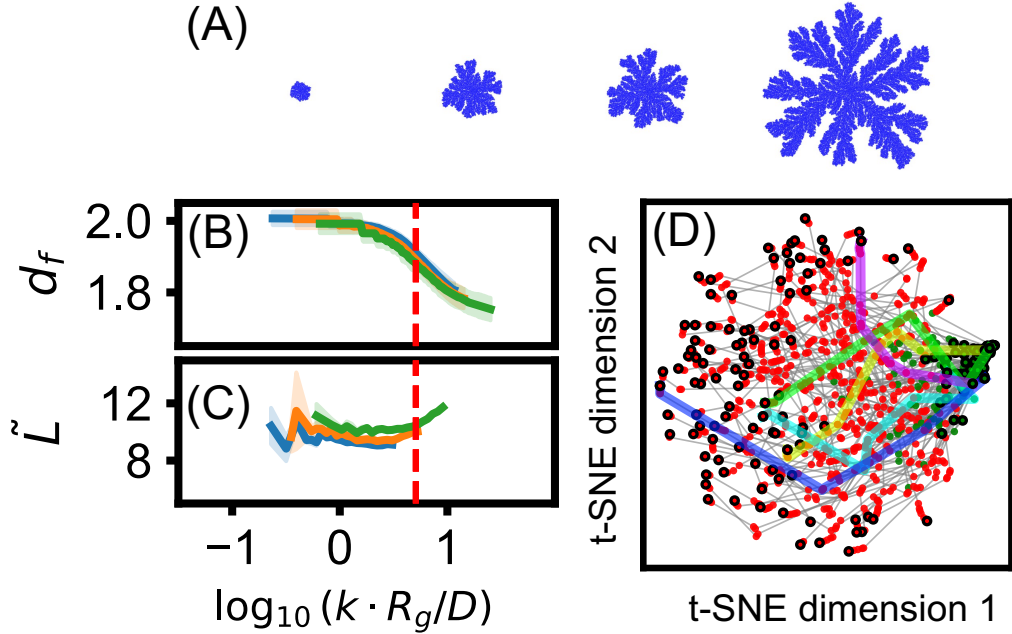


FIG. 2. Morphological characterization across the compact-to-dendritic transition (CDT). (A) Representative electrodeposition morphologies during growth at $\log_{10} k = -1.69$. (B) Fractal dimension d_f (Eq. 3) as a function of growth progression. (C) Dimensionless interfacial length \tilde{L}_{int} (Eq. 6) as a function of growth progression. Panels (B) and (C) present results for three reaction rates, $\log_{10} k = -1.69$ (green), -1.90 (orange), and -2.12 (blue). As a visual reference, red dashed lines indicate the CDT at $R_g = R_c$. Here, the ensemble-averaged value of R_c is adopted, reported in Ref. 47. (D) Two-dimensional t-SNE embedding of 100 growth trajectories at $\log_{10} k = -1.69$ constructed from the e_{phys} representations. Markers with black edges denote the starting and end points of each trajectory, and marker color indicates the morphological state: green for compact growth and red for dendritic growth. Grey lines connect each trajectory. Thick colored lines show five representative growth trajectories in the latent space.

defining $D_c = T_c - T \geq 0$, sequences are alarm-negative for $D_c \geq E$ and alarm-positive otherwise. No input sequence used for prediction contains images from the post-CDT regime. The triplet (L_s, E, D_c) characterizes historical context, prediction horizon, and earliness. All models are trained and evaluated using identical (L_s, E) and data splits. We stress that, because the label assignment explicitly depends on the prediction horizon E , a separate model must be trained for each value of E . Otherwise, an identical input sequence of length L_s could be labeled as either alarm-positive or alarm-negative, leading to an ill-posed learning problem.

To prevent temporal leakage, data splitting is performed at the level of independent simulation runs rather than individual sequences. The full dataset is first partitioned into a training set (80%) and a held-out test set (20%). The training set is then further divided into five folds with an internal 4:1 ratio for training and validation, enabling five-fold cross-validation, corresponding to approximately 64% training, 16% validation, and 20% testing data overall. Stratification is applied to preserve class balance. In total, we use 200 independent growth trajectories, each consisting of 1000 images. Final performance metrics are obtained by evaluating each fold-trained model and reporting the average across folds. For all models tested, learning curves for both training and validation decreases well within 30 epochs.

A. CNN–GRU architecture

We employ a hybrid CNN–GRU architecture that learns spatiotemporal representations directly from raw image sequences in an end-to-end manner^{103,104}. The model explicitly separates spatial pattern extraction, handled by a convolutional neural network (CNN)⁸⁹, from temporal dependency modeling, handled by gated recurrent units (GRUs)¹⁰⁵. This separation reflects the multiscale nature of dendritic growth dynamics, in which localized morphological patterns evolve over time and collectively give rise to macroscopic instability. The overall model f_θ can be written as

$$f_\theta^{\text{CNN-GRU}}(I_t) = \text{MLP}(\text{GRU}(\text{CNN}(I_t))), \quad (7)$$

where θ denotes the set of learnable parameters, and the multilayer perceptron (MLP) is used for final binary event-prediction.

Each frame I_t is processed independently by a CNN encoder,b

$$F_t = \text{CNN}(I_t) \in \mathbb{R}^{S_F \times (H_F \times W_F)}, \quad (8)$$

where the encoder consists of three convolutional blocks followed by adaptive average pooling to a fixed spatial resolution. The resulting feature map F_t contains S_F feature channels resolved over a $H_F \times W_F$ grid of coarse spatial bins. Unless noted

otherwise, the main results in this work use $H_F \times W_F = 1 \times 1$ and $S_F = 16$, corresponding to global spatial pooling that emphasizes feature-type information over explicit spatial localization. Flattening yields a frame-level embedding $e_t = \text{vec}(F_t)$.

The sequence of embeddings $\{e_t\}_{t=T-L_s+1}^T$ is then fed into a gated recurrent unit,

$$h_t = \text{GRU}(h_{t-1}, e_t) \in \mathbb{R}^{H_d}, \quad (9)$$

where H_d denotes the hidden-state dimension. The GRU produces a sequence of hidden states $H = \{h_t\}_{t=T-L_s+1}^T$, from which the final hidden state h_T is used as a compact summary of the input sequence. This final hidden state is mapped to a scalar logit,

$$\hat{y} = \text{MLP}(h_T), \quad (10)$$

which represents the unnormalized confidence for the alarm-positive class.

The CNN-GRU model is trained end-to-end using a weighted binary cross-entropy loss¹⁰⁶ with logits, implemented as `BCEWithLogitsLoss` in PyTorch (version 2.4.1)⁸⁷. Optimization is performed with the AdamW optimizer¹⁰⁷. Regularization includes batch normalization¹⁰⁸, dropout¹⁰⁹, gradient clipping¹¹⁰, and early stopping¹¹¹, together with a ReduceLROnPlateau scheduler for adaptive learning-rate control. PyTorch implementations of all models investigated in this work are publicly available at Ref. 112.

B. Alternative spatial and temporal encoding models

Regarding spatial encoding, in addition to the CNN-based representation, we employ a complementary encoding motivated by the physical characterization of deposition growth (Eq. 2). For each time frame t , the physics-informed encoder, denoted Rad^{phys} , computes the radial density gradient from the center of the image I_t . This procedure yields a physics-based feature vector e_t^{phys} of dimension $F^{47,103}$,

$$e_t^{\text{phys}} = \text{Rad}^{\text{phys}}(I_t), \quad (11)$$

$$= \frac{d}{dR} \left[\frac{N(R)}{\pi R^2} \right] \in \mathbb{R}^F. \quad (12)$$

Similar to the CNN encoder, this representation coarsens the underlying spatial information; however, it does so through explicitly defined, physically interpretable quantities rather than learned convolutional filters. We note that e_t^{phys} may also be constructed from alternative physically motivated descriptors beyond those considered in this work.

To assess the role of temporal integration in the CNN-GRU framework, we consider several alternative temporal models. As non-temporal baselines, we employ a linear regressor (LR)¹¹³ and a MLP^{114,115}, both of which operate on the same frame-level input features but lack explicit mechanisms for integrating information across time. The linear regressor provides a purely linear reference, whereas the MLP allows for nonlinear feature transformations without modeling temporal dependencies.

| Model | Spatial | Temporal | Notes |
|--------------------------|---------------------|----------|---------------------------|
| CNN-GRU | CNN | GRU | End-to-end spatiotemporal |
| CNN-TCN | CNN | TCN | End-to-end spatiotemporal |
| CNN ^{cl} -GRU | CNN ^{cl} | GRU | Fixed spatial |
| CNN ^{cl} -LR | CNN ^{cl} | LR | Linear static baseline |
| CNN ^{cl} -MLP | CNN ^{cl} | MLP | Nonlinear static baseline |
| Rad ^{phys} -GRU | Rad ^{phys} | GRU | Physics-informed spatial |
| Rad ^{phys} -MLP | Rad ^{phys} | MLP | Physics-informed spatial |
| CNN-LR | CNN | LR | End-to-end |
| CNN-MLP | CNN | MLP | End-to-end |

TABLE I. Summary of model architectures and their spatial and temporal components.

In addition, we consider a temporal convolutional network (TCN)¹¹⁶⁻¹¹⁸ as an alternative deep-learning model for temporal integration. Unlike recurrent architectures that accumulate information through hidden-state memory, the TCN aggregates temporal context via convolutional filtering along the time axis³³⁻³⁵. This comparison enables us to distinguish whether the performance gains of the CNN-GRU primarily arise from recurrent memory or from temporal integration more generally, independent of the specific architectural realization. All models tested in this work are summarized in Table I.

IV. RESULTS AND DISCUSSION

In this section, we present results for early-warning prediction of CDTs. We first characterize morphological signatures of the transition using physics-based descriptors, which serve as ground truth for the prediction task. We then quantitatively compare the performance of early-warning models, highlighting the necessity of end-to-end spatiotemporal learning for reliable prediction near the CDT. Next, we analyze the learned latent hidden-state dynamics of the CNN-GRU to assess their interpretation as low-dimensional surrogates for morphological evolution. Finally, we examine the transferability of the learned representations across different reaction-rate conditions, which turns out to be limited but systematic.

A. Identification of morphological signatures across the CDT

We first examine how compact-to-dendritic transitions (CDTs) manifest in physics-based morphological descriptors and physics-derived feature representations (Fig. 2). This analysis establishes physically grounded signatures of the transition that serve as a reference for subsequent early-warning prediction and model comparison, while also highlighting the pronounced heterogeneity across individual growth trajectories.

A growing deposit undergoes a morphological crossover from compact to dendritic growth across the CDT (Fig. 2A). To quantify this crossover, we consider the fractal dimension d_f , which provides a robust and sensitive measure of mor-

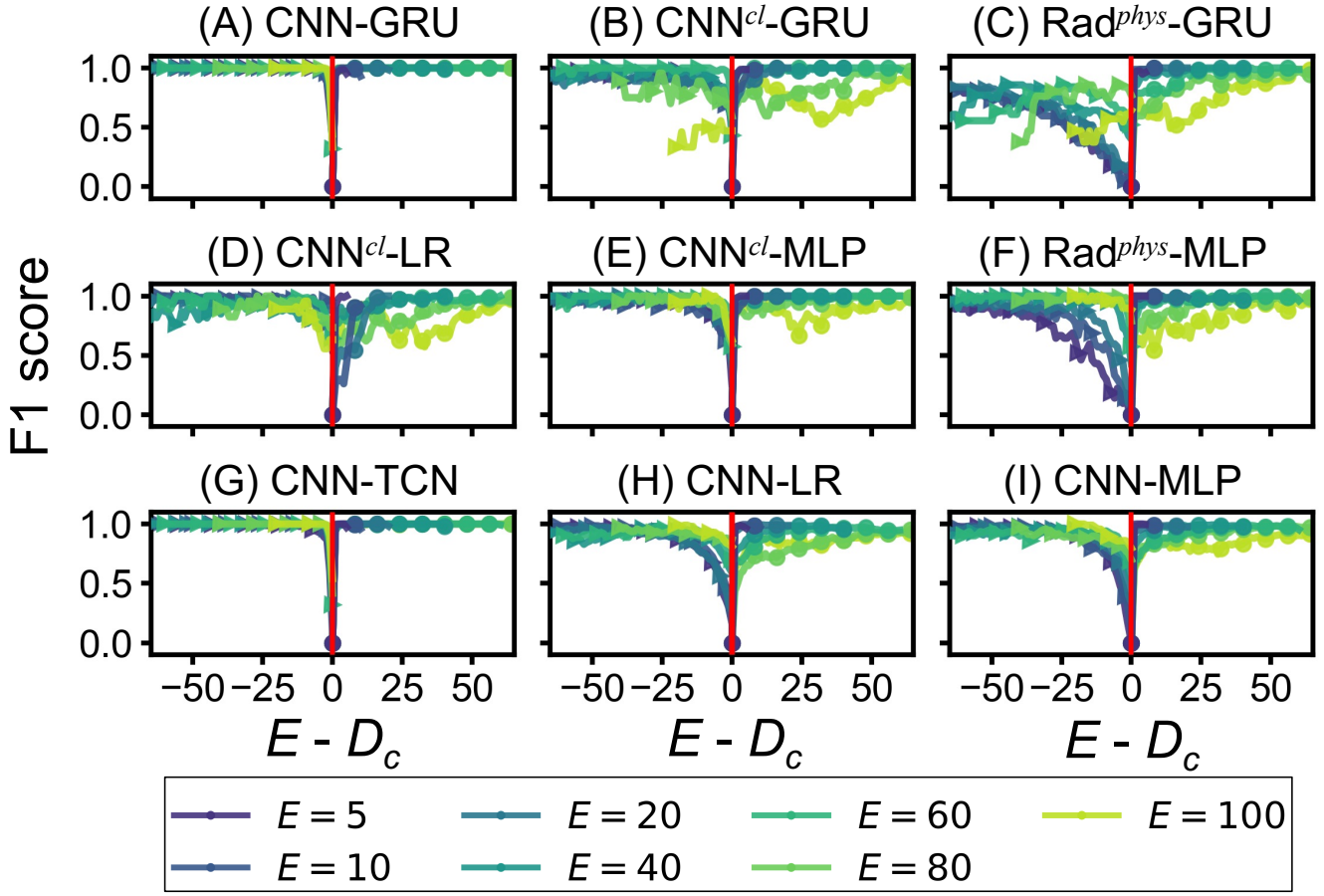


FIG. 3. F1-score performance of early-warning models as a function of $E - D_c$ at $L_s = 5$. Circle and triangle markers denote the F1-positive and F1-negative scores, respectively (Eq. 13). Here, $D_c = T_c - T$ is the temporal distance between the prediction time and the trajectory-specific transition point, and E is the prediction horizon. $E \leq D_c$ corresponds to the alarm-negative (compact) regime, whereas $E > D_c$ corresponds to the alarm-positive regime. D_c is determined using the sequence-specific R_c . Panels A, G, H, and I correspond to end-to-end learning models. Red vertical lines denote the boundaries between the two early-warning prediction regimes. The grid resolution ($H \times W = 32 \times 32$), CNN feature dimension ($S_F = 16$), and global spatial pooling size ($H_F \times W_F = 1 \times 1$) are fixed across all models.

phological evolution across the transition (Fig. 2B). Consistent with previous studies⁴⁷, an appropriate renormalization of the growth variables yields a unified description of the CDT across different reaction rates. For all values of k considered ($\log_{10} k \in \{-2.12, -1.90, -1.69\}$), growth initially proceeds in a compact manner and subsequently transitions to a dendritic morphology beyond a critical radius R_c ⁴⁷. The location of the transition depends systematically on k , with higher reaction rates leading to earlier transitions and dendritic growth emerging at smaller aggregate sizes. We again note that the value of diffusion coefficient D is held fixed throughout this work.

As shown in Fig. 2C, the dimensionless interfacial length \tilde{L}_{int} also exhibits a gradual crossover across the CDT. It responds sensitively to the regime near and beyond R_c through an increase in magnitude, reflecting the emergence of ramified, dendritic interfaces relative to compact growth. Other physics-based descriptors, including circularity, aspect ratio, and convex hull ratio, display similar trends (Fig. A2 in the Appendix); however, their variations across R_c are compara-

tively smooth and strongly correlated, limiting their ability to unambiguously localize the transition at the level of individual trajectories.

Despite the well-defined R_c observed at the ensemble-averaged level, individual growth trajectories exhibit substantial heterogeneity due to the inherently stochastic nature of the deposition process. This heterogeneity is illustrated in Fig. 2D, which shows a two-dimensional t-SNE embedding of the physics-derived feature vectors e_{phys} (Eq. 11) constructed from all trajectories. No learning is involved in this representation, as e_{phys} consists solely of hand-crafted, physics-motivated descriptors. While trajectories remain relatively clustered in the compact regime, a pronounced spread emerges in the dendritic regime, reflecting the diversity of post-CDT morphologies. Such variability complicates the assignment of morphological states based solely on an ensemble-averaged R_c . Accordingly, we employ trajectory-resolved transition points R_c (Eq. 4) as ground truth labels for the supervised early-warning models considered below.

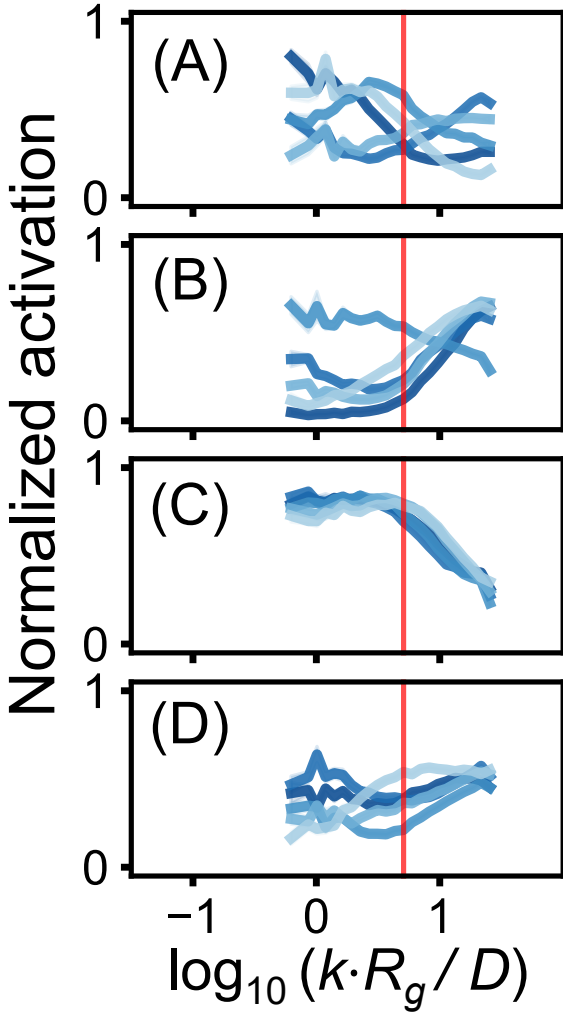


FIG. 4. Normalized activation of the five most important spatial features e_t for $E = 5$ during growth at $\log_{10} k = -1.69$: (A) CNN-GRU, (B) CNN^{cl} , (C) Rad^{phys} , and (D) CNN-TCN. As a visual reference, red vertical lines indicate the CDT at $R_g = R_c$, adopting the ensemble-averaged value of R_c reported in Ref. 47. Bluer colors indicate features with higher importance score.

B. The CNN-GRU enables early-warning prediction of the CDT

The early-warning task evaluates how reliably each method can anticipate the onset of dendritic growth given an observation window of length L_s and a future prediction horizon E , which together define the temporal distance D_c between the prediction time and the sequence-specific transition time T_c (Fig. 1). Performance is quantified using two types of F1

scores¹¹⁹: $\text{F1}_{\text{positive}}$ and $\text{F1}_{\text{negative}}$, defined as

$$\text{F1}_{\text{positive}} = \frac{\text{TP}}{\text{TP} + \frac{1}{2}(\text{FP} + \text{FN})}, \quad (13)$$

$$\text{F1}_{\text{negative}} = \frac{\text{TN}}{\text{TN} + \frac{1}{2}(\text{FN} + \text{FP})}.$$

Here, TP, FP, TN, and FN denote the numbers of true positives, false positives, true negatives, and false negatives, respectively. For each value of E , the F1 scores are computed over the ensemble of test sequences.

Figure 3 summarizes both F1 scores (Eq. 13) for binary forecasting of growth trajectories at $\log_{10} k = -1.69$ with fixed $L_s = 5$, plotted as a function of $E - D_c$. In this representation, D_c specifies the location of the true transition relative to the prediction time, while $E - D_c$ determines the expected label: $E - D_c < 0$ corresponds to the alarm-negative regime, $E - D_c > 0$ to the alarm-positive regime, and $E - D_c = 0$ marks the alarm-boundary. By construction, $\text{F1}_{\text{positive}}$ primarily reflects performance in the alarm-positive regime, whereas $\text{F1}_{\text{negative}}$ emphasizes performance in the alarm-negative regime. Although the sequence label (alarm) depends only on the sign of $E - D_c$, the conditional distribution of pre-transition morphologies at fixed $E - D_c$ changes with E because of different temporal proximity-to-CDT.

All models exhibit better performance in temporal regions far from $E \approx D_c$ than in the vicinity of $E \approx D_c$ in both regimes, consistent with the fact that the early-warning task is most challenging near the CDT, where morphological precursors are weak and buried by intrinsic fluctuations. For the same value of $E - D_c$, the F1 performance further depends on E : in the alarm-negative regime relative to E , prediction is relatively easy for small E , whereas in the alarm-positive regime relative to E , prediction becomes easier for large E .

Beyond these general trends, the F1 performance exhibits clear model-specific differences, highlighting the importance of simultaneous spatiotemporal learning together with effective temporal information integration. The CNN-GRU model (Fig. 3A) consistently outperforms all other approaches, with the CNN-TCN (Fig. 3G) achieving comparable F1 scores. Notably, in the most challenging region near the alarm-boundary, only the CNN-GRU and CNN-TCN maintain high F1 scores across a broad range of prediction horizons. This indicates that effective temporal integration is not limited to a specific recurrent-memory mechanism.

Models that incorporate temporal modeling but rely on fixed or separately learned spatial representations (CNN^{cl} -GRU and Rad^{phys} -GRU; see Figs. 3B–C) underperform their LR and MLP counterparts and remain systematically inferior to the CNN-GRU. For the same temporal modeling, CNN^{cl} outperforms Rad^{phys} in the vicinity of $E = D_c$ in both regimes. Rad^{phys} tends to suffer in detecting challenging cases near T_c , misclassifying a late-stage compact morphology as alarm-positive and an early-stage dendritic morphology as alarm-negative. Consequently, Rad^{phys} exhibits high false alarms for both positive and negative when $E \approx D_c$. Regarding temporal learning alone, MLP outperforms LR, as expected,

primarily by reducing false-negative alarms when $E \gtrsim D_c$. These results demonstrate that temporal modeling alone is insufficient without jointly optimized spatial representations.

Models that employ simultaneous spatiotemporal learning without effective temporal integration (Figs. 3H–I) also show degraded performance, particularly in the vicinity of $E = D_c$ in both regimes (see Fig. A3 in the Appendix for a magnified view). Therefore, reliable early-warning with a wide prediction horizon near the CDT requires the co-implementation of two essential components: (i) temporal integration and (ii) simultaneous end-to-end learning of spatial representations. The likelihood results before thresholding further support this conclusion, showing the overwhelming performance of both CNN–GRU and CNN–TCN models (see Fig. A4 in the Appendix).

We further examine the effect of spatial resolution in the CNN–GRU model by varying the CNN feature size (S_F) and the degree of spatial pooling ($H_F \times W_F$) (Figs. A5 and A6 in the Appendix). While all configurations achieve strong F1-score performance, increasing spatial detail through larger S_F or $H_F \times W_F$ leads to system-dependent changes in the likelihood results. Notably, these modifications do not systematically enhance early-warning prediction and, in some cases, degrade performance as reflected in the likelihood analysis. For example, for $S_F = 16$ (as in Fig. 3), the likelihood remains similar or even deteriorates as $H_F \times W_F$ increases. This nonmonotonic behavior indicates a trade-off between preserving fine spatial detail and maintaining a compact, noise-robust representation.

C. Spatiotemporal learning with CNN–GRU provides early-warning signals of the CDT

The importance of simultaneous spatiotemporal learning is further underscored by the temporal evolution of the learned spatial features e_t . For interpretability, we additionally compute activations and latent trajectories over the full growth trajectory (including post-CDT frames). Figures 4 display the normalized activation $a_t \in [0, 1]$ of the five most important spatial features e_t for $E = 5$, obtained via min–max normalization (see Appendix D for details). All models exhibit changes in feature activations across the CDT, but their characteristic behaviors and predictive utility differ. We note that the activation patterns exhibit only weak dependence on the prediction horizon E (see Fig. A7 in the Appendix).

The physics-derived features e_{phys} exhibit activations that remain nearly constant in the pre-CDT regime and then drop rapidly after R_c (Fig. 4C). This behavior closely resembles the evolution of the fractal dimension d_f , which likewise shows little sensitivity prior to R_c . Similarly, the feature activations of CNN^{cl} closely mirror the behavior of \tilde{L}_{int} (Fig. 4B): they remain near zero in the pre-CDT regime and increase sharply only after R_c . This reflects that CNN^{cl} is trained for static compact–dendritic classification and therefore primarily responds to more developed post-transition morphologies. Such ReLU-like responses are insufficiently structured to provide reliable early-warning capability in the regime of weak precursors prior to the CDT.

By contrast, the CNN–GRU exhibits qualitatively distinct activation patterns (Fig. 4A). A subset of features evolves gradually within the alarm-negative regime, indicating sensitivity to progressive morphological destabilization, while other features display pronounced peaks prior to R_c , signaling the impending transition. We interpret these pre-transition peaks as being suggestive of the emergence of localized interfacial instabilities that are insufficient to produce a globally dendritic morphology but nevertheless indicate a loss of compact-growth stability. Such precursors are weak, spatially localized, and strongly history-dependent, rendering them difficult to identify from single-frame descriptors. Their accumulation through temporal integration provides a natural explanation for the superior early-warning capability of the CNN–GRU¹⁹. Moreover, the relatively uniform importance across e_t features supports that early morphological precursors of the CDT are not encoded in a single dominant spatial motif, but are instead distributed over multiple subtle and heterogeneous local patterns, consistent with the need for a distributed spatiotemporal representation.

Saliency analysis provides complementary qualitative insight into the physical content of the learned spatial features by highlighting input regions that most strongly influence the model predictions^{120–122}. Near R_c , the most salient pixels are predominantly concentrated along the deposit interface, with additional contributions in the surrounding region, indicating sensitivity to both interfacial morphology and aggregate extent (see Fig. A8 in the Appendix). These results further support that the spatial features encode physically meaningful aspects of the evolving growth morphology.

While individual feature activations differ markedly between the models, the global geometric organization of trajectories in the embedding space is similar: the two-dimensional t-SNE embeddings of growth trajectories constructed from e_t closely resemble the structure observed for the physics-derived representation e_{phys} (see Fig. A9 A in the Appendix). In all latent spaces, growth trajectories form a compact-regime core and subsequently radiate into a heterogeneous dendritic manifold, reflecting the stochastic and history-dependent nature of dendritic growth. We note that, for the CNN–GRU, the global spatial pooling resolution ($H_F \times W_F$) at a given feature dimension (S_F) can alter the latent-space manifolds, as it controls the amount of spatial information retained in e_t . In general, finer spatial decomposition tends to yield improved separation between compact and dendritic manifolds in the t-SNE space (see Fig. A9 in the Appendix).

D. Hidden state as a surrogate for morphological evolution

To test whether it serves as a surrogate for the evolving morphological state, we examine the latent-space dynamics of the GRU hidden state h_t , in line with prior work showing that learned latent representations can compactly encode and forecast complex physical dynamics^{96,97,101}. Figure 5 shows the magnitude of the hidden-state velocity, $v_t^h = \|h_t - h_{t-1}\|$, during growth for three GRU-based models: CNN–GRU, CNN^{cl} –GRU, and Rad^{phys} –GRU. We also include the CNN–TCN,

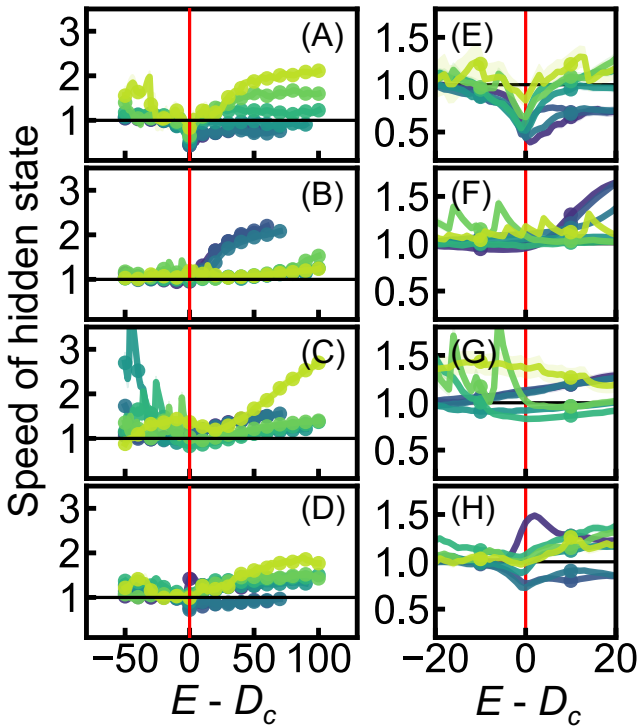


FIG. 5. Latent-space speed during growth at $\log_{10} k = -1.69$. (A–C) Hidden-state velocity $v_t^h = \|h_t - h_{t-1}\|$ for the GRU-based models: (A) CNN-GRU, (B) CNN^{cl}-GRU, and (C) Rad^{phys}-GRU. (D) Latent speed $v_t^C = \|c_t - c_{t-1}\|$ for the CNN-TCN model, computed from the feature vector c_t of the final hidden layer. (E–H) Magnified views of the regions near the transition point T_c for panels (A–D), respectively. Different colors indicate different values of E , consistent with the color coding in Fig. 3. Red vertical lines denote the boundaries between the two early-warning prediction regimes, and black horizontal lines serve as guides to the eye.

which has no recurrent hidden state. In this case, we compute an analogous latent speed, $v_t^C = \|c_t - c_{t-1}\|$, using the feature vector c_t from the final hidden layer of the TCN, which plays a role analogous to that of h_t in the GRU. Results are displayed as a function of $E - D_c$, consistent with the early-warning performance shown in Fig. 3.

Similar to the activation behavior of e_t , the latent-space speed exhibits markedly model-specific trends. For the CNN-GRU, the hidden-state dynamics shows pronounced changes near the alarm-boundary, spanning both alarm-positive and alarm-negative regions for all investigated values of E (Fig. 5A). This behavior closely mirrors the trends observed in the activations of the learned spatial features, which also capture signatures in both regimes. It is notable that a reduction of v_t^h upon approaching the transition from either regime is suggestive of a phenomenology qualitatively reminiscent of slowing-down observed in some complex systems^{19,53} (Fig. 5E).

Moreover, in the alarm-negative regime, v_t^h collapses onto a single curve for most values of E , whereas it diverges in the alarm-positive regime. This behavior is consistent with the

structure observed in the t-SNE embeddings. The resulting E -dependent divergence in the post-CDT regime implies that capturing local morphological features requires increasingly fine spatial resolution, reflecting the strong heterogeneity of dendritic morphologies across growth trajectories. Consistent behavior is observed upon varying $H_F \times W_F$: finer spatial bins lead to enhanced collapse in the post-CDT regime, indicating improved capture of local morphological evolution (See Fig. A12 in the Appendix).

In contrast, the CNN^{cl}-GRU and Rad^{phys}-GRU models exhibit hidden-state dynamics that change primarily in the alarm-positive regime, consistent with their corresponding feature-activation patterns (Figs. 5B and C). For CNN^{cl}-GRU at small E , v_t^h displays a ReLU-like response across the alarm boundary, with appreciable changes emerging mainly after $E = D_c$. At large E , v_t^h shows little variation across the alarm boundary, while appreciable changes in latent dynamics mainly emerge in the alarm-positive regime. The Rad^{phys}-GRU exhibits only modest variations in v_t^h across the alarm boundary, making the transition difficult to identify from the hidden-state dynamics alone.

Overall, these observations suggest that the hidden state of the CNN-GRU provides a low-dimensional surrogate for the evolving morphological state, capturing the progressive destabilization of compact growth prior to the emergence of a fully dendritic morphology. From this perspective, the CNN-GRU can be viewed as performing an implicit coarse-graining of the high-dimensional growth dynamics, mapping microscopic morphological fluctuations onto a low-dimensional latent trajectory. This interpretation further supports the importance of simultaneous spatiotemporal learning for early-warning prediction of the CDT.

At the same time, the emergence of meaningful latent-space dynamics does not rely uniquely on the presence of a recurrent unit. The latent-space speed of the CNN-TCN (Figs. 5D and H) also exhibits systematic changes near the alarm-boundary, qualitatively similar—though less pronounced—to the slowing-down behavior observed for the GRU-based models. This suggests that the key ingredient is the end-to-end spatiotemporal learning framework itself, rather than a specific choice of temporal integration mechanism.

E. Transferability to other reaction-rate conditions: Limited yet systematic

Finally, we evaluate the CNN-GRU model trained at $\log_{10} k = -1.69$ under two additional reaction-rate conditions, $\log_{10} k = -1.90$ and -2.12 , which correspond to slower reaction kinetics and therefore a later onset of the CDT during growth. As shown in Fig. 2B–C, CDTs arising under different reaction–diffusion conditions can be collapsed onto a single renormalized representation based on statistical-mechanical scaling relations. Such collapse might suggest that a model trained under one condition could generalize across reaction and diffusion rates.

In contrast to this physics-motivated expectation, the CNN-GRU model pre-trained at $\log_{10} k = -1.69$ exhibits

limited transferability to other reaction-rate conditions, albeit in a systematic manner (see Fig. A10 in the Appendix). As the reaction rate departs from the training condition toward $\log_{10} k = -1.90$ and -2.12 , the F1-score performance degrades substantially.

For $\log_{10} k = -1.90$, the F1-negative score in the alarm-negative regime remains relatively high and decreases systematically with increasing E . In contrast, performance in the alarm-positive regime deteriorates more strongly. At $\log_{10} k = -2.12$, forecasting performance degrades severely in both alarm-negative and alarm-positive regimes.

This systematic, k -dependent transferability is further reflected in the latent-state dynamics. For $\log_{10} k = -1.90$, the latent-space speed of the hidden state exhibits a slowing-down behavior near the alarm boundary similar to that of the pre-trained case, but lacks sufficient resolution to reliably pinpoint the boundary at $E = D_c$. For $\log_{10} k = -2.12$, the latent dynamics no longer show a meaningful reorganization around the alarm boundary, consistent with the strongly degraded predictive performance.

Although fine-tuning the pre-trained model at $\log_{10} k = -1.69$ restores strong predictive performance in both cases (see Fig. A11 in the Appendix), we find no evidence for accelerated learning during fine-tuning. These results suggest that, despite the statistical-mechanical collapse of the CDT under reaction-rate rescaling, the learned latent representation does not inherit this invariance. Consequently, reliable forecasting appears to require explicit retraining for each reaction-rate condition. A more detailed analysis of this limitation is left for future work.

V. CONCLUSIONS AND FUTURE DIRECTIONS

In this work, we investigated compact-to-dendritic transitions (CDTs) in a controlled particle-based electrodeposition model and formulated an explicit early-warning prediction problem based on trajectory-resolved transition points. By combining physics-based growth simulations with image-based spatiotemporal learning, we demonstrated that early-warning of dendritic instability is intrinsically a spatiotemporal problem: neither static morphological descriptors nor temporal learning built on predefined features alone provide reliable precursors. Instead, end-to-end learning of joint spatial and temporal representations (CNN-GRU and CNN-TCN) enables robust anticipation of the transition over extended prediction horizons.

Analysis of learned features and hidden-state dynamics further indicates that the CNN-GRU constructs a low-dimensional surrogate of the evolving morphological state, consistent with an implicit coarse-graining of nonequilibrium growth dynamics. We further showed that this learned spatiotemporal representation exhibits limited but systematic transferability across reaction-rate conditions, with predictive performance degrading as the inference condition departs from the training condition, consistent with corresponding changes in latent-state dynamics.

Several directions merit future investigation. A natural extension of the present two-dimensional framework is to three-

dimensional deposition, where morphological complexity and heterogeneity are further amplified and early detection of incipient instabilities is even more challenging. Hybrid approaches that combine learned spatiotemporal representations with physics-informed features may improve interpretability while retaining high early-warning performance. Extending the framework to experimental imaging data, including noisy or partially observed interfaces, will be essential for practical deployment.

Physically informed early-warning and control strategies may ultimately provide an important component for electrochemical energy-storage systems operating near their stability limits. Achieving this goal requires the ability to characterize and interpret latent-state dynamics, opening a pathway toward dynamic control of nonequilibrium growth processes. If the latent state indeed tracks the evolving morphological state, it could serve as a compact surrogate for feedback and closed-loop control, enabling charging or deposition protocols to be adaptively modulated to steer the system away from catastrophic dendritic growth^{48,94,95}.

Appendix A: Particle-based model for electrodeposition in two dimensions

Battery charging is a complex process involving multiple coupled molecular phenomena, including bulk and interfacial ion diffusion and electroreduction^{46–48}. In this work, we intentionally simplify this process by modeling electrodeposition as particle-based aggregation in 2D⁴⁷, represented as a sequence of stochastic aggregation events. Each event consists of two elementary processes: Brownian diffusion of a reactive particle in the electrolyte domain and a probabilistic deposition reaction upon contact with the growing aggregate. The latter represents the electrochemical reduction at the battery interface (e.g., $\text{Li}^+ + e^- \rightarrow \text{Li}^0$ in the case of a lithium metal battery). In this work, we adopt a publicly available implementation of the model and the parameters provided in Ref. 102.

Brownian diffusion. Following Ref. 47, an algorithmic treatment is employed to enhance computational efficiency while preserving the correct diffusive statistics. Reactive particles are launched from a bounding surface enclosing the existing aggregate and undergo Brownian motion governed by a diffusion coefficient D . When a particle is far from the aggregate, its motion is accelerated using a first-passage jump scheme. Specifically, if the minimum distance H between the particle and the aggregate exceeds a cutoff distance σ_{cut} , the particle is displaced by a uniformly distributed jump of radius $d_{\text{jump}} = H - \varepsilon$, where ε is a small numerical buffer. Once the particle enters the near-field region ($H \leq \sigma_{\text{cut}}$), its motion is resolved explicitly via Gaussian-distributed displacements,

$$\mathbf{r}(t + \Delta t) = \mathbf{r}(t) + \mathcal{N}(0, 2D\Delta t \mathbf{I}), \quad (\text{A1})$$

where Δt denotes the simulation time step.

Deposition reaction. If a collision with the aggregate is

detected, a deposition reaction occurs with probability

$$P = k \sqrt{\frac{\pi \Delta t}{D}}, \quad (\text{A2})$$

where k is the reaction rate constant. With probability P , the particle irreversibly sticks to the aggregate and becomes part of the growing deposit; otherwise, it undergoes elastic reflection and continues diffusing⁴⁷. This probabilistic sticking rule allows the model to continuously interpolate between reaction-limited growth ($P \ll 1$), which produces compact morphologies, and diffusion-limited growth ($P \rightarrow 1$), which leads to dendritic structures. In this work, we vary only the reaction rate constant k while keeping all other parameters fixed, enabling a systematic investigation of morphological instabilities associated with the compact-to-dendritic transition in electrodeposition⁴⁷.

Appendix B: 2D growth images using grid representation

The particle coordinates are discretized onto a fixed square grid to obtain binary occupancy images, where occupied and unoccupied pixels represent the presence or absence of deposited particles. The spatial bounds are determined using the complete particle set to ensure consistent spatial scaling across all time points. The projected coordinates are then mapped onto a $H \times W$ grid, following a global coordinate normalization. In this work, we only use square grids with $H = W$.

$$\text{coord}_{\text{norm}} = \frac{\text{coord} - \text{min}_{\text{bound}}}{\text{range}_{\text{bound}}}, \quad (\text{B1})$$

which ensures that all images share a common spatial reference frame. A reference configuration containing 10^6 particles is used to define the global normalization and scaling parameters, which are applied consistently across all growth stages.

A physical length scale is further defined as

$$\text{scale} = \frac{\min(x_{\text{range}}, y_{\text{range}})}{\text{grid size}}, \quad (\text{B2})$$

allowing conversion between pixel units and physical distances in subsequent quantitative analyses.

This grid-based representation G provides a standardized and scale-consistent description of evolving deposition morphologies, enabling direct quantitative comparison of spatial patterns and ensuring compatibility with both physics-based diagnostics and data-driven learning methods (Fig. A1). The same image construction, normalization, and spatial scaling procedures are applied consistently throughout this work.

Appendix C: Physics-based characterization

We quantify aggregate morphologies using a set of interrelated, physically interpretable descriptors, including the fractal

dimension, interfacial length, circularity, aspect ratio, and convex hull ratio. Except for the fractal dimension, all physical quantities are computed from the binary grid images using OpenCV (version 4.11.0.86).

Fractal dimension, d_f : The fractal dimension characterizes the global scaling properties of the aggregate through the relation in Eq. 2 in the main text. In practice, the derivative to compute d_f in Eq. 3 in the main text is evaluated using a sliding-window approach centered at each particle count, incorporating data from ± 4 neighboring sampling steps. The step size is chosen as $\max(5,000, N/8)$ to balance numerical stability and computational efficiency. To suppress unphysical values arising statistical noise, the estimated values are restricted to $1.5 \leq d_f \leq 2.2$, corresponding to physically realistic ranges for two-dimensional diffusion-limited aggregation.

Interfacial length, L : The interfacial length is defined as the total perimeter of the aggregate and provides a measure of surface roughness and branching complexity. The perimeter is extracted from binary occupancy images using Canny edge detection, as implemented in OpenCV, with parameters $\sigma = 2.0$, $\text{low_threshold} = 50$, and $\text{high_threshold} = 150$. The pixel-based perimeter is converted to physical units using the spatial scale factor defined in Eq. B2.

Circularity, C : Circularity quantifies the compactness of the aggregate shape and is defined as

$$C = \frac{4\pi A}{P^2}, \quad (\text{C1})$$

where A is the area of the aggregate and P is its perimeter. A perfect circle yields $C = 1$, whereas irregular or fractal structures exhibit smaller values. Circularity is computed from the contours of the binary grid representation and provides a simple geometric measure of morphological irregularity.

Aspect ratio, AR: The aspect ratio characterizes directional anisotropy in aggregate growth. Principal component analysis (PCA) is applied to the spatial distribution of occupied grid points to extract the major and minor principal axes. The aspect ratio is defined as the ratio of the minor-axis length to the major-axis length. Values significantly smaller than unity indicate elongated or directionally biased growth, whereas values close to unity correspond to isotropic morphologies.

Convex hull ratio, CHR: The convex hull ratio quantifies branching and porosity of the aggregate and is defined as

$$\text{CHR} = \frac{A}{A_{\text{CH}}}, \quad (\text{C2})$$

where A_{CH} denotes the area of the convex hull. Lower values of CHR indicate more branched and fractal morphologies, while values approaching unity correspond to compact, space-filling growth.

Appendix D: Computation of normalized activation and feature importance

Each input image is processed by a CNN with $S_F = 16$ channels, and each channel output is reduced to a scalar activation

| Parameter | Symbol | Value | Description |
|------------------------|-----------------------|-------------------------------------|--------------------------------|
| Reaction rate constant | k | $10^{-1.69}, 10^{-1.9}, 10^{-2.12}$ | Controls sticking probability |
| Diffusion coefficient | D | 1.0 | Particle diffusion coefficient |
| Particle radius | a | 1.0 | Effective particle radius |
| Time step | Δt | 10^{-3} | Brownian integration step |
| Cutoff distance | σ_{cut} | $10 a$ | Far-/near-field threshold |
| Numerical buffer | ε | $10^{-3} a$ | Jump-distance stabilizer |
| System size | L | $1024 a$ | Simulation box size |
| Total particle number | N_{total} | 10^6 | Particles per realization |

TABLE A1. Simulation parameters used in the particle-based electrodeposition model.

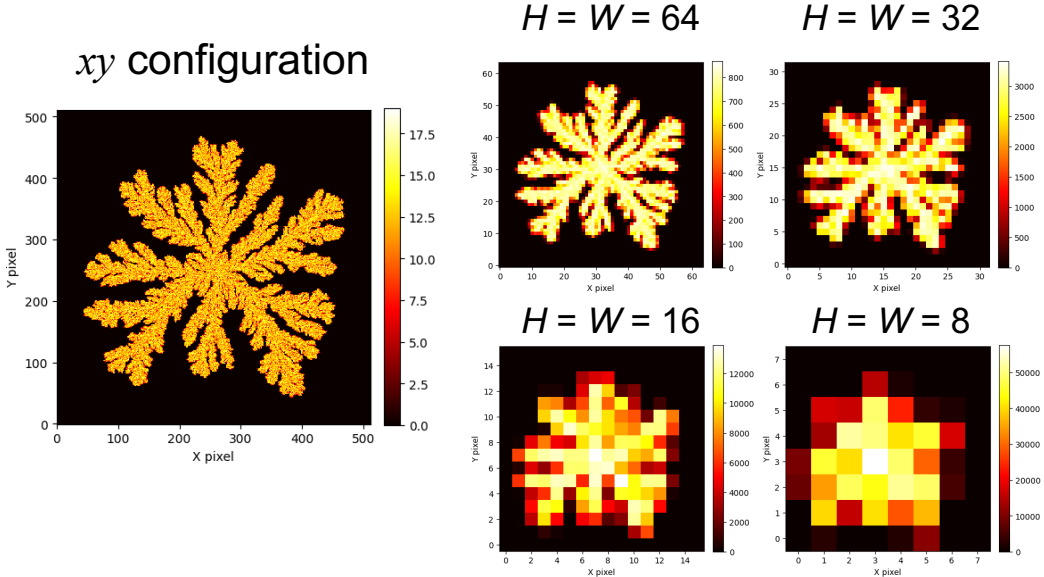


FIG. A1. Grid-based representation of the growth images. The colorbar indicates the particle density in each pixel for different spatial resolutions $H \times W$.

e_c through global average pooling over spatial dimensions. To facilitate comparisons across samples, we normalize activations channel-wise over the full dataset as

$$\tilde{e}_c^{(n)} = \frac{e_c^{(n)} - \min_k e_c^{(k)}}{\max_k e_c^{(k)} - \min_k e_c^{(k)}} \in [0, 1], \quad (\text{D1})$$

where n labels samples and k runs over all samples.

The normalized activations are examined as a function of the control parameter $\log_{10}(k R_g / D)$, which is discretized into 50 uniform bins. Within each bin b and for each channel c , we compute the mean $\mu_{c,b}$ and standard deviation $\sigma_{c,b}$ of \tilde{e}_c .

Channel relevance is quantified using gradient-based saliency. Specifically, we define an importance score

$$I_c = \mathbb{E} \left[\left\| \frac{\partial \hat{y}}{\partial \mathbf{F}_c} \right\| \right], \quad (\text{D2})$$

where \hat{y} denotes the model output and \mathbf{F}_c the feature map of channel c . Channels are ranked according to I_c , and the five most important channels are chosen and visualized.

¹R. M. May, “Thresholds and breakpoints in ecosystems with a multiplicity of stable states,” *Nature* **269**, 471–477 (1977).

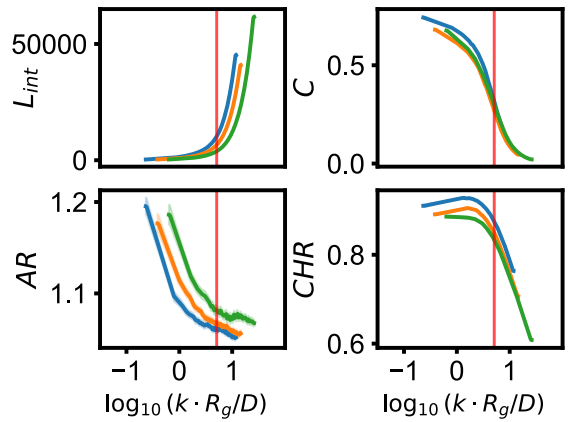


FIG. A2. Physical characterizations, including interfacial length (L_{int}), circularity (C), aspect ratio (AR), and convex hull ratio (CHR). As a visual reference, red vertical lines indicate the CDT at $R_g = R_c$, adopting the ensemble-averaged value of R_c reported in Ref. 47.

²J. Meibohm and M. Esposito, “Finite-time dynamical phase transition in

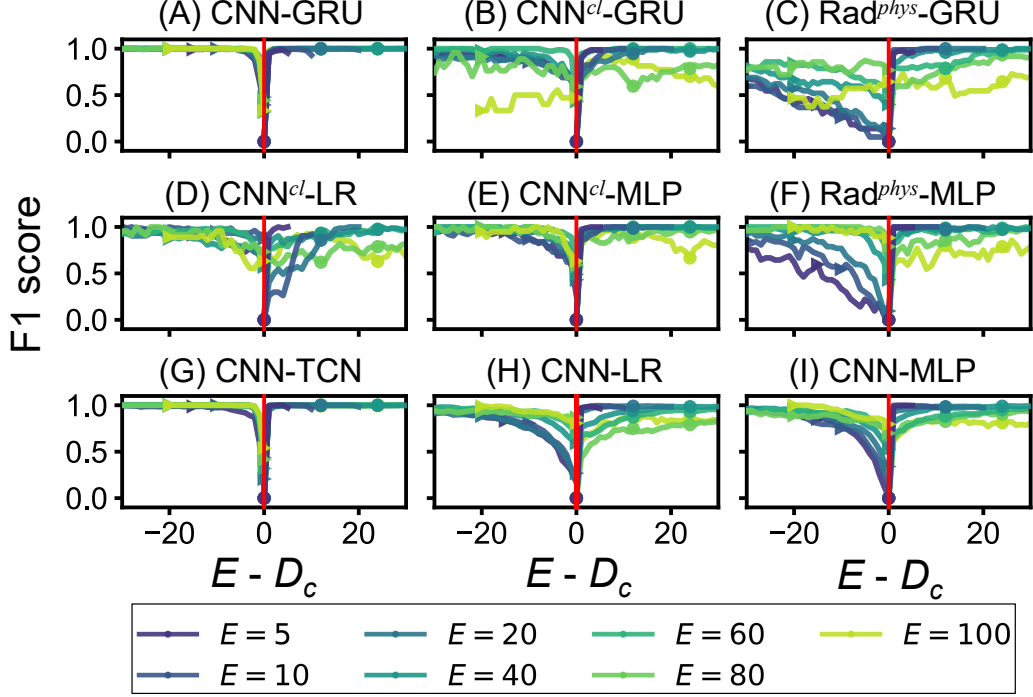


FIG. A3. F1-score performance of early-warning models as a function of $E - D_c$ at $L_s = 5$. Circle and triangle markers denote the F1-positive and F1-negative scores, respectively. The panels show magnified views of the corresponding results in Fig. 3 of the main text.

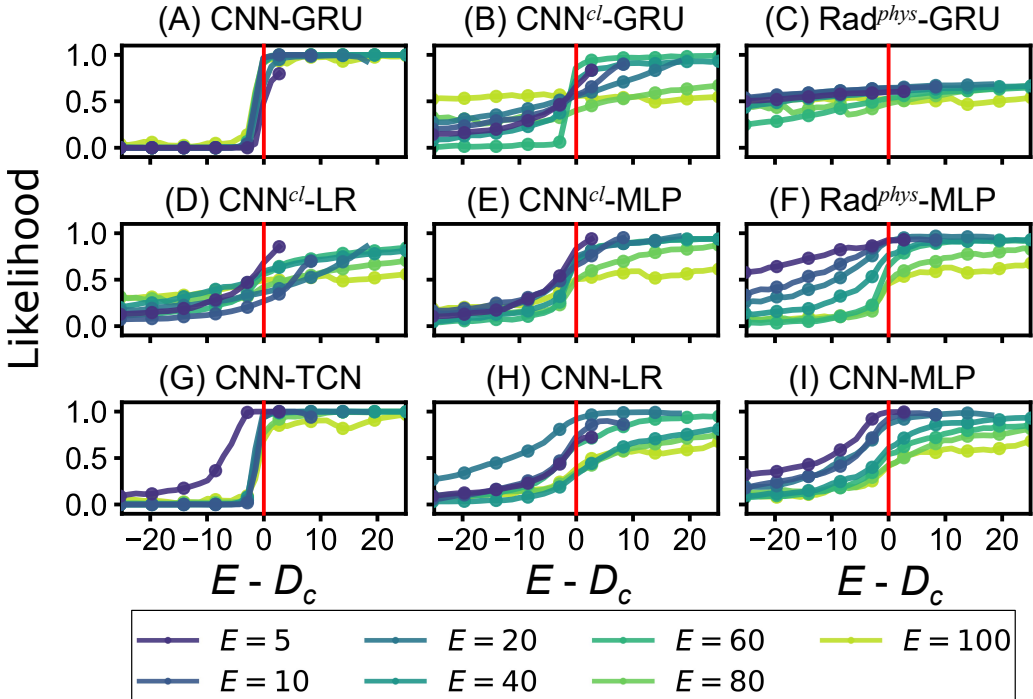


FIG. A4. Likelihood evaluation of early-warning models as a function of $E - D_c$ at $L_s = 5$. The panels show the corresponding results in Fig. 3 of the main text.

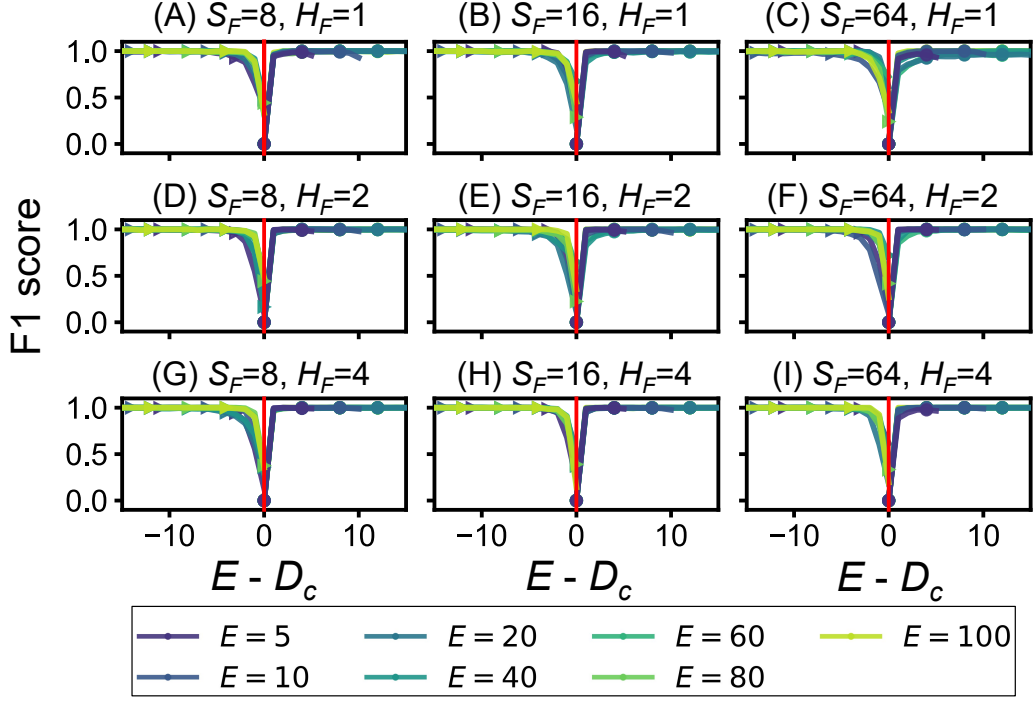


FIG. A5. F1-score performance of early-warning models as a function of $E - D_c$ at $L_s = 5$ with varying spatial information: CNN feature dimension S_F and global spatial pooling $H_F \times W_F$. Circle and triangle markers denote the F1-positive and F1-negative scores, respectively. Here, $H_F = W_F$.

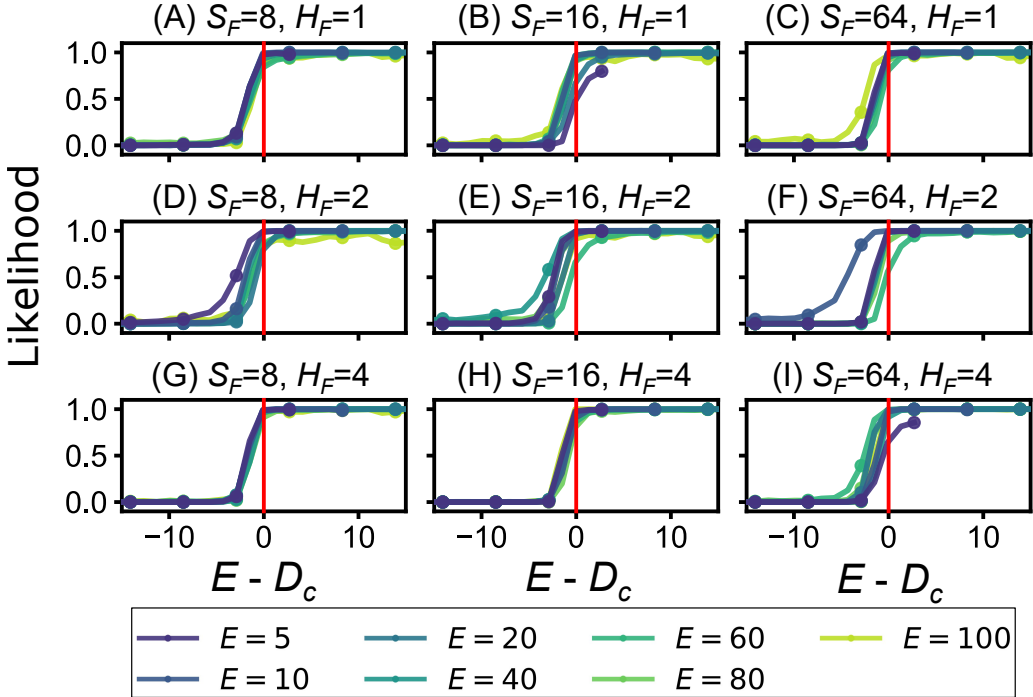


FIG. A6. Likelihood evaluation of early-warning models as a function of $E - D_c$ at $L_s = 5$ with varying spatial information: CNN feature dimension S_F and global spatial pooling $H_F \times W_F$. Here, $H_F = W_F$. The panels show the corresponding results in Fig. A5.

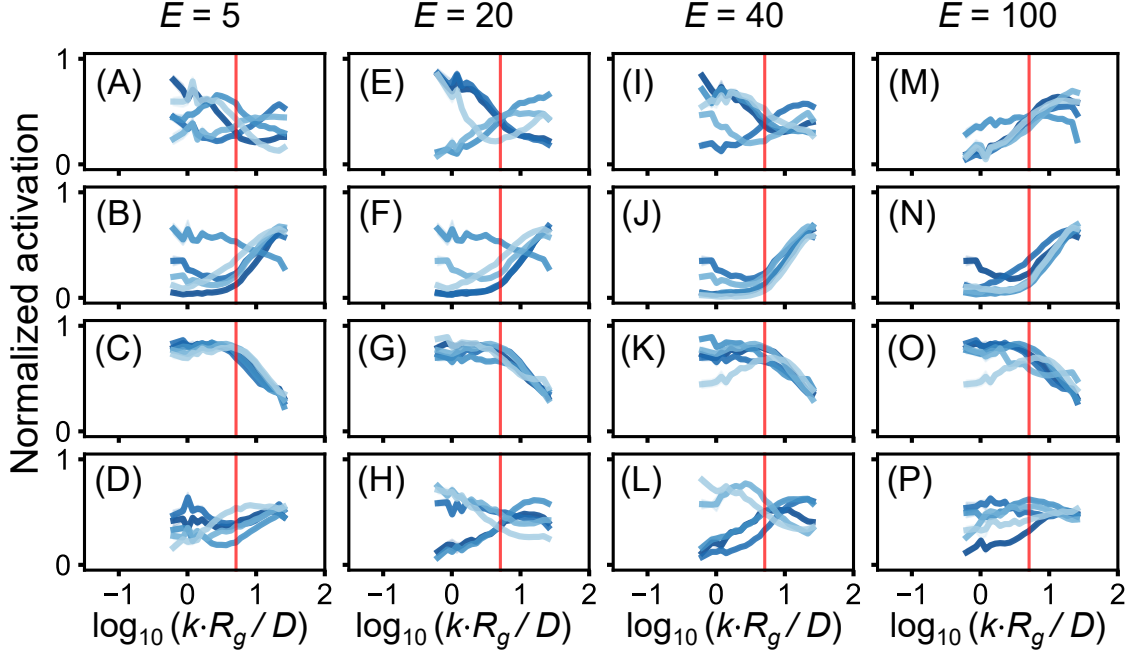


FIG. A7. Normalized activation of spatial features e_t for different prediction horizons E during growth at $\log_{10} k = -1.69$. (A,E,I,M) CNN–GRU, (B,F,J,N) CNN^{cl} , (C,G,K,O) Rad^{phys} , and (D,H,L,P) CNN–TCN. Results for $E = 5$ correspond to Fig. 4 in the main text. As a visual reference, red vertical lines indicate the CDT at $R_g = R_c$, adopting the ensemble-averaged value of R_c reported in Ref. 47. Bluer colors indicate features with higher importance scores.

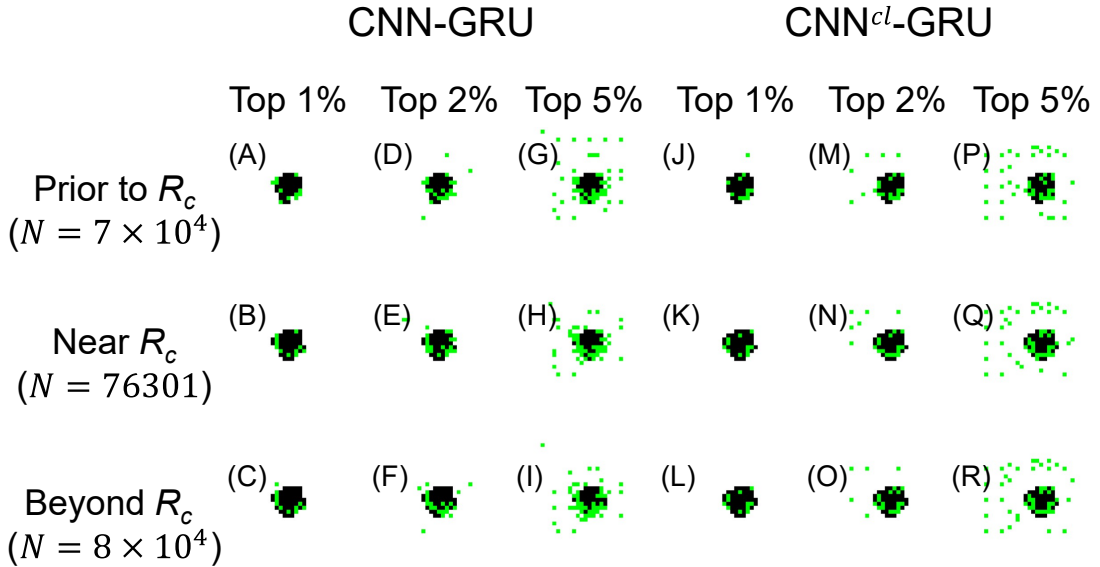


FIG. A8. Saliency analysis of CNN features using guided backpropagation. Deposit pixels are shown in black, while pixels with high saliency are highlighted in bright green.

nonequilibrium relaxation,” Phys. Rev. Lett. **128**, 110603 (2022).

³M. Heyl, A. Polkovnikov, and S. Kehrein, “Dynamical quantum phase transitions in the transverse-field Ising model,” Phys. Rev. Lett. **110**, 135704 (2013).

⁴J. P. Garrahan, R. L. Jack, V. Lecomte, E. Pitard, K. van Duijvendijk, and F. van Wijland, “Dynamical first-order phase transition in kinetically

constrained models of glasses,” Phys. Rev. Lett. **98**, 195702 (2007).

⁵N. Vadakkayil, M. Esposito, and J. Meibohm, “Critical fluctuations at a finite-time dynamical phase transition,” Phys. Rev. E **110**, 064156 (2024).

⁶G. Ódor, “Universality classes in nonequilibrium lattice systems,” Rev. Mod. Phys. **76**, 663–724 (2004).

⁷C. E. Fiore, P. E. Harunari, C. E. F. Noa, and G. T. Landi, “Current

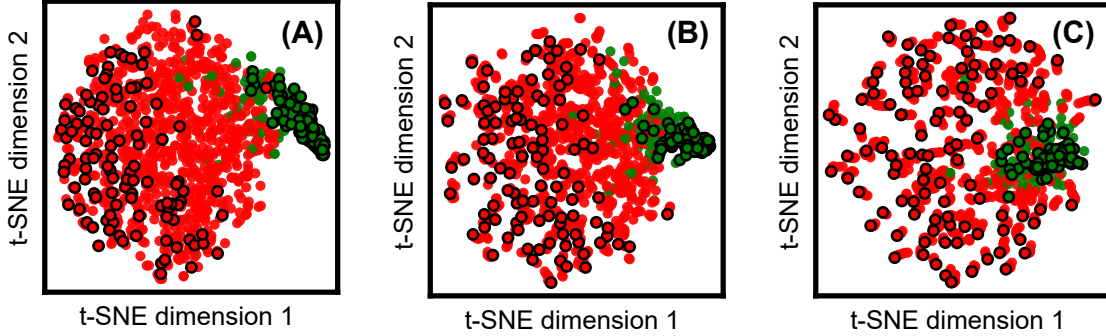


FIG. A9. Two-dimensional t-SNE embeddings of 100 growth trajectories at $\log_{10} k = -1.69$ constructed from e_t of the CNN–GRU model. The panels correspond to Fig. 3A in the main text and show different global spatial pooling resolutions: (A) 1×1 , (B) 2×2 , and (C) 4×4 . Markers with black edges denote the starting and end points of each trajectory, and marker color indicates the morphological state: green for compact growth and red for dendritic growth.

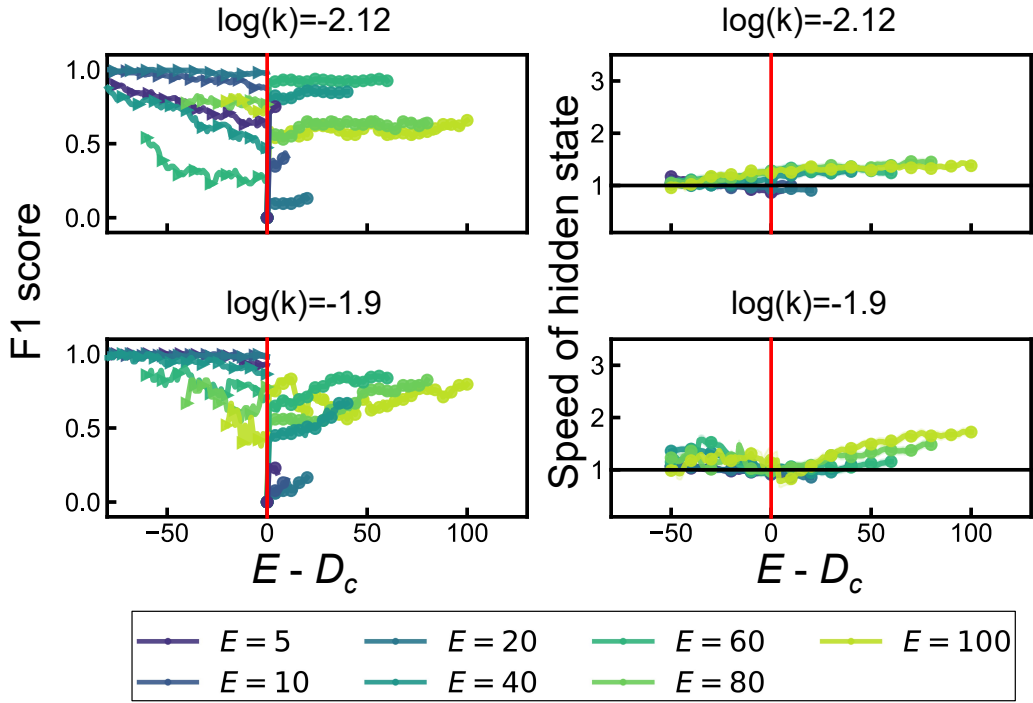


FIG. A10. Transfer inference using a CNN–GRU model without fine-tuning. The model is pre-trained at $\log_{10} k = -1.69$, corresponding to Fig. 3 in the main text.

fluctuations in nonequilibrium discontinuous phase transitions,” Phys. Rev. E **104**, 064123 (2021).

⁸R. Biggs, S. R. Carpenter, and W. A. Brock, “Turning back from the brink: Detecting an impending regime shift in time to avert it,” Proceedings of the National Academy of Sciences **106**, 826–831 (2009).

⁹N. Marsal, L. Weicker, D. Wolfersberger, and M. Sciamanna, “Bistability controlled by convection in a pattern-forming system,” Phys. Rev. Lett. **118**, 013902 (2017).

¹⁰A. Deger, A. Lazarides, and S. Roy, “Constrained dynamics and directed percolation,” Phys. Rev. Lett. **129**, 190601 (2022).

¹¹H. Hinrichsen, A. Jiménez-Dalmaroni, Y. Rozov, and E. Domany, “Flowing sand: A physical realization of directed percolation,” Phys. Rev. Lett. **83**, 4999–5002 (1999).

¹²S. Zapperi, P. Ray, H. E. Stanley, and A. Vespignani, “Avalanches in breakdown and fracture processes,” Phys. Rev. E **59**, 5049–5057 (1999).

¹³M. Kardar, G. Parisi, and Y.-C. Zhang, “Dynamic scaling of growing interfaces,” Phys. Rev. Lett. **56**, 889–892 (1986).

¹⁴Y. Cho and W. M. Jacobs, “Nonequilibrium interfacial properties of chemically driven fluids,” The Journal of Chemical Physics **159**, 154101 (2023).

¹⁵V. Démery and E. Fodor, “Driven probe under harmonic confinement in a colloidal bath,” Journal of Statistical Mechanics: Theory and Experiment **2019**, 033202 (2019).

¹⁶A. Pagare and B. J. Cherayil, “Stochastic thermodynamics of a harmonically trapped colloid in linear mixed flow,” Physical Review E **100**, 052124 (2019).

¹⁷I. Buttinoni, L. Caprini, L. Alvarez, F. J. Schwarzenbach, and H. Löwen,

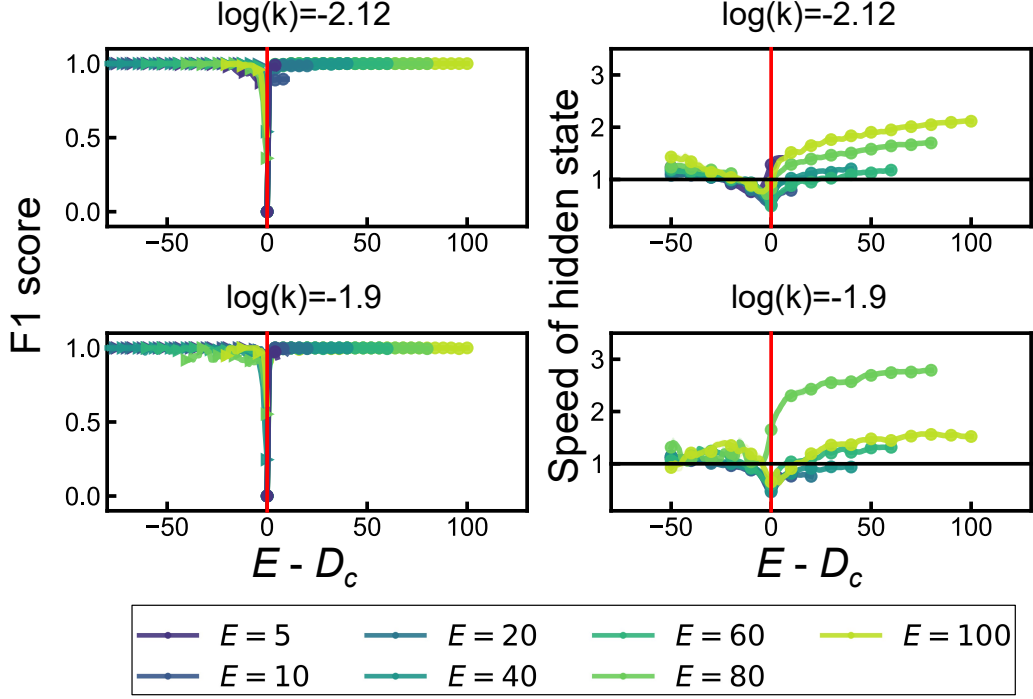


FIG. A11. Transfer inference using a CNN-GRU model with fine-tuning. The model is pre-trained at $\log_{10} k = -1.69$, corresponding to Fig. 3 in the main text.

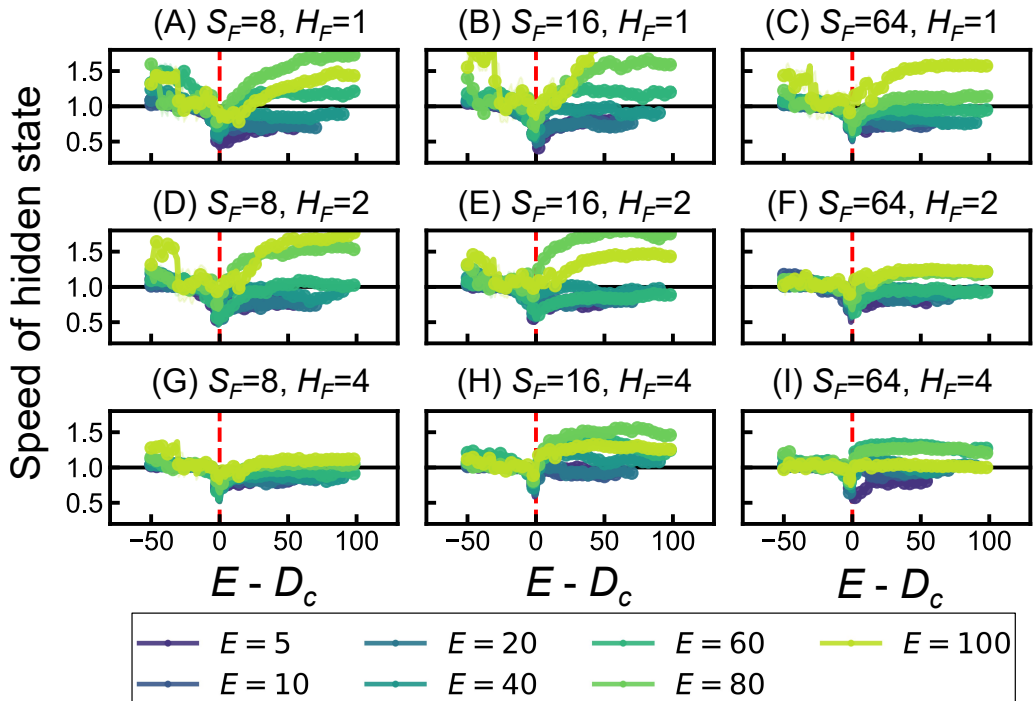


FIG. A12. Latent-space speed of hidden hidden state during growth with varying spatial information: CNN feature dimension S_F and global spatial pooling $H_F \times W_F$. Here, $H_F = W_F$. The panels show the corresponding results in Figs. A5 and A6.

"Active colloids in harmonic optical potentials ^(a)," *Europhysics Letters* **140**, 27001 (2022).

¹⁸M. Faran and G. Bisker, "Nonequilibrium Self-Assembly Control by the Stochastic Landscape Method," *Journal of Chemical Information and Modeling* **65**, 4067–4080 (2025).

¹⁹M. Scheffer, J. Bascompte, W. A. Brock, V. Brovkin, S. R. Carpenter, V. Dakos, H. Held, E. H. Van Nes, M. Rietkerk, and G. Sugihara, "Early-warning signals for critical transitions," *Nature* **461**, 53–59 (2009).

²⁰T. M. Bury, R. I. Sujith, I. Pavithran, M. Scheffer, T. M. Lenton, M. Anand, and C. T. Bauch, "Deep learning for early warning signals of tipping points," *Proceedings of the National Academy of Sciences* **118** (2021).

²¹B. M. S. Arani, S. R. Carpenter, L. Lahti, E. H. van Nes, and M. Scheffer, "Exit time as a measure of ecological resilience," *Science* **372**, eaay4895 (2021).

²²K. Hock, A. Hastings, C. Doropoulos, R. C. Babcock, J. C. Ortiz, A. Thompson, and P. J. Mumby, "Transient dynamics mask the resilience of coral reefs," *Theoretical Ecology* **17**, 1–12 (2024).

²³V. Stolbova, E. Surovyatkina, B. Bookhagen, and J. Kurths, "Tipping elements of the Indian monsoon: Prediction of onset and withdrawal," *Geophysical Research Letters* **43**, 3982–3990 (2016).

²⁴Y. Zheng and N. Boers, "Mean exit times as global measure of resilience of tropical forest systems under climatic disturbances—analytical and numerical results," *Chaos: An Interdisciplinary Journal of Nonlinear Science* **33**, 113136 (2023).

²⁵D. I. A. McKay, A. Staal, J. F. Abrams, R. Winkelmann, B. Sakschewski, S. Loriani, I. Fetzer, S. E. Cornell, J. Rockström, and T. M. Lenton, "Exceeding 1.5°C global warming could trigger multiple climate tipping points," *Science* **377**, eabn7950 (2022).

²⁶B. M. Flores, E. Montoya, B. Sakschewski, N. Nascimento, A. Staal, R. A. Betts, C. Levis, D. M. Lapola, A. Esquivel-Muelbert, C. Jakovac, C. A. Nobre, R. S. Oliveira, L. S. Borma, D. Nian, N. Boers, S. B. Hecht, H. ter Steege, J. Arieira, I. L. Lucas, E. Berenguer, J. A. Marengo, L. V. Gatti, C. R. C. Mattos, and M. Hirota, "Critical transitions in the Amazon forest system," *Nature* **626**, 555–564 (2024).

²⁷X. Zhang, Y. Xu, Q. Liu, and J. Kurths, "Tipping of thermoacoustic systems with secondary bifurcation in colored noise environments: Effects of rate," *Chaos: An Interdisciplinary Journal of Nonlinear Science* **35**, 033124 (2025).

²⁸J. Ma, D. Li, R. Wang, Q. Liu, Y. Xu, T. Kapitaniak, and J. Kurths, "Predicting tipping phenomenon in a conceptual airfoil structure under extreme flight environment," *Journal of Sound and Vibration* **618**, 119306 (2025).

²⁹G. Wang and X. Zou, "Qualitative analysis of critical transitions in complex disease propagation from a dynamical systems perspective," *International Journal of Bifurcation and Chaos* **26**, 1650239 (2016).

³⁰M. Hirota, M. Holmgren, E. H. V. Nes, and M. Scheffer, "Global resilience of tropical forest and savanna to critical transitions," *Science* **334**, 232–235 (2011).

³¹J. Ma, Y. Xu, Y. Li, R. Tian, and J. Kurths, "Predicting noise-induced critical transitions in bistable systems," *Chaos: An Interdisciplinary Journal of Nonlinear Science* **29**, 081102 (2019).

³²Y. Meng, J. Jiang, C. Grebogi, and Y.-C. Lai, "Noise-enabled species recovery in the aftermath of a tipping point," *Phys. Rev. E* **101**, 012206 (2020).

³³A. Aryanfar, M. R. Hoffmann, and W. A. Goddard, "Finite-pulse waves for efficient suppression of evolving mesoscale dendrites in rechargeable batteries," *Physical Review E* **100**, 042801 (2019).

³⁴I. Jang and A. Yethiraj, "Effect of diffusion constant on the morphology of dendrite growth in lithium metal batteries," *The Journal of Chemical Physics* **154**, 234705 (2021).

³⁵K. N. Wood, E. Kazyak, A. F. Chadwick, K.-H. Chen, J.-G. Zhang, K. Thornton, and N. P. Dasgupta, "Dendrites and Pits: Untangling the Complex Behavior of Lithium Metal Anodes through Operando Video Microscopy," *ACS Central Science* **2**, 790–801 (2016).

³⁶S. R. Carpenter and W. A. Brock, "Rising variance: a leading indicator of ecological transition," *Ecology Letters* **9**, 311–318 (2006).

³⁷P. Ditlevsen and S. Ditlevsen, "Warning of a forthcoming collapse of the atlantic meridional overturning circulation," *Nature Communications* **14**, 4254 (2023).

³⁸V. Guttal and C. Jayaprakash, "Changing skewness: an early warning signal of regime shifts in ecosystems," *Ecology Letters* **11**, 450–460 (2008).

³⁹R. Radhakrishnan, I. Pavithran, V. Livina, J. Kurths, and R. I. Sujith, "Early warnings are too late when parameters change rapidly," *Scientific Reports* **15**, 20256 (2025).

⁴⁰R. Wang, J. A. Dearing, P. G. Langdon, E. Zhang, X. Yang, V. Dakos, and M. Scheffer, "Flickering gives early warning signals of a critical transition to a eutrophic lake state," *Nature* **492**, 419–422 (2012).

⁴¹L. Xu, D. Patterson, A. C. Staver, S. A. Levin, and J. Wang, "Unifying deterministic and stochastic ecological dynamics via a landscape-flux approach," *Proceedings of the National Academy of Sciences* **118**, e2103779118 (2021).

⁴²M. Dijkstra and E. Luijten, "From predictive modelling to machine learning and reverse engineering of colloidal self-assembly," *Nature Materials* **20**, 762–773 (2021).

⁴³Z. Liu, X. Zhang, X. Ru, T.-T. Gao, J. M. Moore, and G. Yan, "Early predictor for the onset of critical transitions in networked dynamical systems," *Phys. Rev. X* **14**, 031009 (2024).

⁴⁴J. Ma, Y. Cui, R. Wang, J. Feng, Y. Xu, and J. Kurths, "Early warning of noise-induced critical transitions in two-dimensional ecosystems," *Chaos: An Interdisciplinary Journal of Nonlinear Science* **36**, 023121 (2026).

⁴⁵M. A. Chowdhury, S. S. Al-Wahaibi, and Q. Lu, "Adaptive safe reinforcement learning-enabled optimization of battery fast-charging protocols," *AICHE Journal* **71**, e18605 (2025).

⁴⁶D. R. MacFarlane, J. Huang, and M. Forsyth, "Lithium-doped plastic crystal electrolytes exhibiting fast ion conduction for secondary batteries," *Nature* **402**, 792–794 (1999).

⁴⁷D. Jacobson and T. F. Miller, "Continuum limit of dendritic deposition," *Physical Review E* **111**, 065506 (2025).

⁴⁸C. P. Nielsen and H. Bruus, "Sharp-interface model of electrodeposition and ramified growth," *Physical Review E* **92**, 042302 (2015).

⁴⁹D. Cao, X. Sun, Q. Li, A. Natan, P. Xiang, and H. Zhu, "Lithium Dendrite in All-Solid-State Batteries: Growth Mechanisms, Suppression Strategies, and Characterizations," *Matter* **3**, 57–94 (2020).

⁵⁰R. Pathak, K. Chen, A. Gurung, K. M. Reza, B. Bahrami, J. Pokharel, A. Baniya, W. He, F. Wu, Y. Zhou, K. Xu, and Q. Qiao, "Fluorinated hybrid solid-electrolyte-interphase for dendrite-free lithium deposition," *Nature Communications* **11**, 93 (2020).

⁵¹Y. Chen, M. Li, Y. Liu, Y. Jie, W. Li, F. Huang, X. Li, Z. He, X. Ren, Y. Chen, X. Meng, T. Cheng, M. Gu, S. Jiao, and R. Cao, "Origin of dendrite-free lithium deposition in concentrated electrolytes," *Nature Communications* **14**, 2655 (2023).

⁵²C. Brissot, M. Rosso, J.-N. Chazalviel, and S. Lascaud, "Dendritic growth mechanisms in lithium/polymer cells," *Journal of Power Sources* **81–82**, 925–929 (1999).

⁵³T. Nagatani and Y. Usami, "Pattern formation in nonlinear diffusion-limited aggregation," *Physical Review A* **39**, 2169–2174 (1989).

⁵⁴M. C. Cross and P. C. Hohenberg, "Pattern formation outside of equilibrium," *Reviews of Modern Physics* **65**, 851–1112 (1993).

⁵⁵P. C. Hohenberg and B. I. Halperin, "Theory of dynamic critical phenomena," *Reviews of Modern Physics* **49**, 435–479 (1977).

⁵⁶J. Hunt, "Pattern formation in solidification," *Science and Technology of Advanced Materials* **2**, 147–155 (2001).

⁵⁷A. Karma and W.-J. Rappel, "Phase-field model of dendritic sidebranching with thermal noise," *Phys. Rev. E* **60**, 3614–3625 (1999).

⁵⁸T. A. Witten and L. M. Sander, "Diffusion-Limited Aggregation, a Kinetic Critical Phenomenon," *Phys. Rev. Lett.* **47**, 1400–1403 (1981).

⁵⁹T. A. Witten and L. M. Sander, "Diffusion-limited aggregation," *Phys. Rev. B* **27**, 5686–5697 (1983).

⁶⁰P. Meakin, *Fractals, Scaling and Growth Far from Equilibrium* (Cambridge University Press, 1998).

⁶¹F. Family and T. Vicsek, "Scaling of the active zone in the eden process on percolation networks and the ballistic deposition model," *Journal of Physics A* **18**, L75–L81 (1985).

⁶²A.-L. Barabási and H. E. Stanley, *Fractal Concepts in Surface Growth* (Cambridge University Press, 1995).

⁶³E. Somfai, L. M. Sander, and R. C. Ball, "Scaling and crossovers in diffusion limited aggregation," *Phys. Rev. Lett.* **83**, 5523–5526 (1999).

⁶⁴T. C. Halsey, "Diffusion-limited aggregation: A model for pattern formation," *Physics Today* **53**, 36–41 (2000).

⁶⁵S. Havlin, B. Trus, A. Bunde, and H. E. Roman, "Phase transition in

diffusion-limited aggregations,” *Physical Review Letters* **63**, 1189–1189 (1989).

⁶⁶M. Nauenberg, R. Richter, and L. M. Sander, “Crossover in diffusion-limited aggregation,” *Physical Review B* **28**, 1649–1651 (1983).

⁶⁷R. Ball, M. Nauenberg, and T. A. Witten, “Diffusion-controlled aggregation in the continuum approximation,” *Physical Review A* **29**, 2017–2020 (1984).

⁶⁸P. Ritchie and J. Sieber, “Early-warning indicators for rate-induced tipping,” *Chaos: An Interdisciplinary Journal of Nonlinear Science* **26**, 093116 (2016).

⁶⁹M. Eden, “A two-dimensional growth process,” *Proceedings of the Fourth Berkeley Symposium on Mathematical Statistics and Probability* **4**, 223–239 (1961).

⁷⁰P. Meakin, “Diffusion-limited aggregation in three dimensions: Results from a new cluster-cluster aggregation model,” *Journal of Colloid and Interface Science* **102**, 491–504 (1984).

⁷¹Y. Saito and H. Müller-Krumbhaar, “Critical phenomena in morphology transitions of growing interfaces,” *Physical Review Letters* **74**, 4325–4328 (1995).

⁷²R. M. Brady and R. C. Ball, “Fractal growth of copper electrodeposits,” *Nature* **309**, 225–229 (1984).

⁷³C. Boettiger and A. Hastings, “Tipping points: From patterns to predictions,” *Nature* **493**, 157–158 (2013).

⁷⁴P. D. Ditlevsen and S. J. Johnsen, “Tipping points: Early warning and wishful thinking,” *Geophysical Research Letters* **37**, L19703 (2010).

⁷⁵T. M. Lenton, H. Held, E. Kriegler, J. W. Hall, W. Lucht, S. Rahmstorf, and H. J. Schellnhuber, “Tipping elements in the earth’s climate system,” *Proceedings of the National Academy of Sciences* **105**, 1786–1793 (2008).

⁷⁶N. Masuda, K. Aihara, and N. G. MacLaren, “Anticipating regime shifts by mixing early warning signals from different nodes,” *Nature Communications* **15**, 1086 (2024).

⁷⁷N. Provatas and K. Elder, “Phase-field methods in materials science and engineering,” Wiley (2010).

⁷⁸R. Ma, D. Cao, C. Zhu, Y. Tian, J. Peng, J. Guo, J. Chen, X.-Z. Li, J. S. Francisco, X. C. Zeng, L.-M. Xu, E.-G. Wang, and Y. Jiang, “Atomic imaging of the edge structure and growth of a two-dimensional hexagonal ice,” *Nature* **577**, 60–63 (2020).

⁷⁹J. Rabault, M. Kuchta, A. Jensen, U. Réglade, and N. Cerardi, “Artificial neural networks trained through deep reinforcement learning discover control strategies for active flow control,” *Physical Review Fluids* **4**, 024608 (2019).

⁸⁰P. García, “A machine learning based control of chaotic systems,” *Chaos, Solitons & Fractals* **155**, 111630 (2022).

⁸¹D. Klotsa and R. L. Jack, “Controlling crystal self-assembly using a real-time feedback scheme,” *The Journal of Chemical Physics* **138**, 094502 (2013).

⁸²A. Aggeli, I. A. Nyrkova, M. Bell, R. Harding, L. Carrick, T. C. B. McLeish, A. N. Semenov, and N. Boden, “Hierarchical self-assembly of chiral rod-like molecules as a model for peptide β -sheet tapes, ribbons, fibrils, and fibers,” *Proceedings of the National Academy of Sciences* **98**, 11857–11862 (2001).

⁸³M. Bukov, A. G. R. Day, D. Sels, P. Weinberg, A. Polkovnikov, and P. Mehta, “Reinforcement learning in different phases of quantum control,” *Physical Review X* **8**, 031086 (2018).

⁸⁴J. Pathak, B. Hunt, M. Girvan, Z. Lu, and E. Ott, “Model-free prediction of large spatiotemporally chaotic systems from data,” *Physical Review Letters* **120**, 024102 (2018).

⁸⁵R. Kumar, T. Dhara, H. Hu, and M. Chakraborty, “Visualization-based prediction of dendritic copper growth in electrochemical cells using convolutional long short-term memory,” *Energy and AI* **10**, 100203 (2022).

⁸⁶D. Bhattacharya, D. C. Kleebhatt, A. Statt, and W. F. Reinhart, “Predicting aggregate morphology of sequence-defined macromolecules with recurrent neural networks,” *Soft Matter* **18**, 5037–5051 (2022).

⁸⁷A. Paszke, S. Gross, F. Massa, A. Lerer, J. Bradbury, G. Chanan, T. Killeen, Z. Lin, N. Gimelshein, L. Antiga, A. Desmaison, A. Kopf, E. Yang, Z. DeVito, M. Raison, A. Tejani, S. Chilamkurthy, B. Steiner, L. Fang, J. Bai, and S. Chintala, “Pytorch: An imperative style, high-performance deep learning library,” in *Advances in Neural Information Processing Systems* (2019).

⁸⁸J. Lu, R. Xiong, J. Tian, C. Wang, and F. Sun, “Deep learning to estimate lithium-ion battery state of health without additional degradation experiments,” *Nature Communications* **14**, 2760 (2023).

⁸⁹Y. LeCun, L. Bottou, Y. Bengio, and P. Haffner, “Gradient-based learning applied to document recognition,” *Proceedings of the IEEE* **86**, 2278–2324 (1998).

⁹⁰A. Krizhevsky, I. Sutskever, and G. E. Hinton, “Imagenet classification with deep convolutional neural networks,” *Commun. ACM* **60**, 84–90 (2017).

⁹¹G. Dong, Y. Feng, Y. Lou, M. Zhang, and J. Wei, “Data-driven fast charging optimization for lithium-ion battery using bayesian optimization with fast convergence,” *IEEE Transactions on Transportation Electrification* **PP** (2023).

⁹²S. Park, A. Pozzi, M. Whitmeyer, H. Perez, W. T. Joe, D. M. Raimondo, and S. Moura, “Reinforcement learning-based fast charging control strategy for li-ion batteries,” *2020 IEEE Conference on Control Technology and Applications (CCTA)*, , 100–107 (2020).

⁹³Z. Wang, H. Wu, L. Sun, X. He, Z. Liu, B. Shao, T. Wang, and T.-Y. Liu, “Improving machine learning force fields for molecular dynamics simulations with fine-grained force metrics,” *The Journal of Chemical Physics* **159**, 035101 (2023).

⁹⁴M. D. Tikekar, L. A. Archer, and D. L. Koch, “Stabilizing electrodeposition in elastic solid electrolytes containing immobilized anions,” *Science Advances* **2**, e1600320 (2016).

⁹⁵S. Choudhury, D. Vu, A. Warren, M. D. Tikekar, Z. Tu, and L. A. Archer, “Confining electrodeposition of metals in structured electrolytes,” *Proceedings of the National Academy of Sciences* **115**, 6620–6625 (2018).

⁹⁶P. R. Vlachas, W. Byeon, Z. Y. Wan, T. P. Sapsis, and P. Koumoutsakos, “Data-driven forecasting of high-dimensional chaotic systems with long short-term memory networks,” *Proceedings of the Royal Society A: Mathematical, Physical and Engineering Sciences* **474**, 20170844 (2018).

⁹⁷J. Pathak, B. Hunt, M. Girvan, Z. Lu, and E. Ott, “Model-free prediction of large spatiotemporally chaotic systems from data,” *Physical Review Letters* **120**, 024102 (2018).

⁹⁸J. Ma, Y. Cui, R. Wang, J. Feng, Y. Xu, and J. Kurths, “Early warning of noise-induced critical transitions in two-dimensional ecosystems,” *Chaos: An Interdisciplinary Journal of Nonlinear Science* **36**, 023121 (2026).

⁹⁹T. Yu, A. Yang, T. Zhang, and S. Yuan, “Quantifying the global stability and transition dynamics of a coupled human–environment system via a landscape-flux approach,” *Chaos: An Interdisciplinary Journal of Nonlinear Science* **35**, 033112 (2025).

¹⁰⁰C. Kuehn, “A mathematical framework for critical transitions: Bifurcations, fast–slow systems and stochastic dynamics,” *Physica D: Nonlinear Phenomena* **240**, 1020–1035 (2011).

¹⁰¹N. Masuda, “Predicting Tipping Points in Complex Systems,” *Physics* **17**, 110 (2024).

¹⁰²D. Jacobson, “Reactive deposition simulation code,” https://github.com/drdrjacobs/reactive_deposition_sim, GitHub repository.

¹⁰³C.-I. Wang, I. Joanito, C.-F. Lan, and C.-P. Hsu, “Artificial neural networks for predicting charge transfer coupling,” *The Journal of Chemical Physics* **153**, 214113 (2020).

¹⁰⁴J. Donahue, L. A. Hendricks, M. Rohrbach, S. Venugopalan, S. Guadarrama, K. Saenko, and T. Darrell, “Long-term recurrent convolutional networks for visual recognition and description,” (2017).

¹⁰⁵K. Cho, B. van Merriënboer, C. Gulcehre, D. Bahdanau, F. Bougares, H. Schwenk, and Y. Bengio, “Learning phrase representations using rnn encoder-decoder for statistical machine translation,” (2014), arXiv:1406.1078 [cs.CL].

¹⁰⁶H. He and E. Garcia, “Learning from imbalanced data,” *Knowledge and Data Engineering, IEEE Transactions on* **21**, 1263 – 1284 (2009).

¹⁰⁷I. Loshchilov and F. Hutter, “Decoupled weight decay regularization,” (2019), arXiv:1711.05101 [cs.LG].

¹⁰⁸S. Ioffe and C. Szegedy, “Batch normalization: Accelerating deep network training by reducing internal covariate shift,” (2015), arXiv:1502.03167 [cs.LG].

¹⁰⁹N. Srivastava, G. Hinton, A. Krizhevsky, I. Sutskever, and R. Salakhutdinov, “Dropout: A simple way to prevent neural networks from overfitting,” *Journal of Machine Learning Research* **15**, 1929–1958 (2014).

¹¹⁰R. Pascanu, T. Mikolov, and Y. Bengio, “On the difficulty of training recurrent neural networks,” in *Proceedings of the 30th International Conference on Machine Learning*, Proceedings of Machine Learning Research, Vol. 28, edited by S. Dasgupta and D. McAllester (PMLR, Atlanta, Georgia, USA,

2013) pp. 1310–1318.

¹¹¹L. Prechelt, “Early stopping - but when?” *Neural Networks: Tricks of the Trade*, , 55–69 (1998).

¹¹²H. Jang, (2026), the GitHub repository will be made publicly available upon publication of the manuscript.

¹¹³C. Bishop, “Pattern recognition and machine learning,” (2006) pp. 140–155.

¹¹⁴D. E. Rumelhart, G. E. Hinton, and R. J. Williams, “Learning representations by back-propagating errors,” *Nature* **323**, 533–536 (1986).

¹¹⁵I. Goodfellow, Y. Bengio, and A. Courville, *Deep Learning* (MIT Press, 2016) <http://www.deeplearningbook.org>.

¹¹⁶S. Bai, J. Z. Kolter, and V. Koltun, “An empirical evaluation of generic convolutional and recurrent networks for sequence modeling,” arXiv **abs/1803.01271** (2018).

¹¹⁷A. Borovykh, S. Bohte, and C. W. Oosterlee, “Temporal convolutional networks applied to energy-related time series forecasting,” *Applied Sciences* **10**, 2322 (2020).

¹¹⁸P. Lara-Benítez, M. Carranza-García, J. M. Luna-Romera, and J. C. Riquelme, “Temporal convolutional networks applied to energy-related time series forecasting,” *Applied Sciences* **10** (2020).

¹¹⁹D. C. Blair, “Information retrieval, 2nd ed. c.j. van rijsbergen. london: Butterworths: 1979: 208 pp. price: \$32.50,” *J. Am. Soc. Inf. Sci.* **30**, 374–375 (1979).

¹²⁰K. Simonyan, A. Vedaldi, and A. Zisserman, “Deep inside convolutional networks: Visualising image classification models and saliency maps,” arXiv preprint arXiv:1312.6034 (2014).

¹²¹M. D. Zeiler and R. Fergus, “Visualizing and understanding convolutional networks,” in *European Conference on Computer Vision (ECCV)* (2014) pp. 818–833.

¹²²R. R. Selvaraju, M. Cogswell, A. Das, R. Vedantam, D. Parikh, and D. Batra, “Grad-cam: Visual explanations from deep networks via gradient-based localization,” in *Proceedings of the IEEE International Conference on Computer Vision (ICCV)* (2017) pp. 618–626.